Journal of Power Sources 331 (2016) 452–461

Contents lists available at ScienceDirect

Journal of Power Sources

journal homepage: www.elsevier.com/locate/jpowsour

Highly stable pyridinium-functionalized cross-linked anion exchange membranes for all vanadium redox flow batteries

L. Zeng [a, b], T.S. Zhao [a, *], L. Wei [a], Y.K. Zeng [a], Z.H. Zhang [a]

[a] Department of Mechanical and Aerospace Engineering, The Hong Kong University of Science and Technology, Clear Water Bay, Kowloon, Hong Kong SAR, China

[b] HKUST Jockey Club Institute for Advanced Study, The Hong Kong University of Science and Technology, Clear Water Bay, Kowloon, Hong Kong SAR, China

HIGHLIGHTS

- Pyridinium-functionalized cross-linked BrPPO were fabricated for VRFBs.
- The AEMs exhibited a low vanadium permeability and an acceptable conductivity.
- The AEMs exhibited a superior chemical stability in an *ex situ* immersion test.
- The VRFBs cycled over 537 cycles with a capacity decay rate of 0.037% cycle^{-1}.

GRAPHICAL ABSTRACT

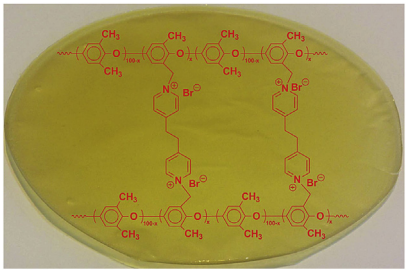

ARTICLE INFO

Article history:
Received 15 August 2016
Received in revised form
6 September 2016
Accepted 12 September 2016
Available online 21 September 2016

Keywords:
Vanadium redox flow battery
Anion exchange membrane
Pyridinium
Chemical stability
Vanadium permeability

ABSTRACT

It has recently been demonstrated that the use of anion exchange membranes (AEMs) in vanadium redox flow batteries (VRFBs) can reduce the migration of vanadium ions through the membrane due to the Donnan exclusion effect among the positively charged functional groups and vanadium ions. However, AEMs are plagued by low chemical stability in harsh chemical environments. Here we propose and fabricate a pyridinium-functionalized cross-linked AEM for VRFBs. The pyridinium-functionalized bromomethylated poly (2,6-dimethyl-1,4-phenylene oxide) exhibits a superior chemical stability as a result of the strengthened internal cross-linking networks and the chemical inertness of the polymer backbone. Therefore, the membrane exhibits littler decay in a harsh environment for 20 days during the course of an *ex situ* immersion test. A cycling test also demonstrates that the VRFB assembled with the membrane enable to retain 80% of the initial discharge capacity over 537 cycles with a capacity decay rate of 0.037% cycle^{-1}. Meanwhile, the membrane also shows a low vanadium permeability and a reasonably high conductivity in supporting electrolytes. Hence, all the measurements and performance tests reported in this work suggest that the membrane is a promising AEM for redox flow batteries to achieve excellent cycling stability and superior cell performance.

1. Introduction

Electrical energy storage (EES) systems are indispensable for the application of future renewable energies as a result of their intermittent and distributed nature [1–4]. Among several categories of EES systems, redox flow batteries (RFBs), which employ metal salts

* Corresponding author.
E-mail address: metzhao@ust.hk (T.S. Zhao).

http://dx.doi.org/10.1016/j.jpowsour.2016.09.065
0378-7753/

[5] or organic components [6,7] with different oxidation states, have been widely investigated due to their significant merits, including flexibility in configuration and operation, long cycle life and high reliability. Among these RFBs, vanadium redox flow batteries (VRFBs) invented by Skyllas-Kazacos in the 1980s have been comprehensively investigated [3]. VRFBs, employing the same vanadium element in four different oxidation states as the redox couples, possess additional merits, such as reduced cross-contamination, high electrochemical activity and suitable polarization potential [8–10].

However, the commercialization of VRFBs has been partially hampered by the ion exchange membranes, which not only preclude the intermixing of positive electrolytes and negative electrolytes, but also allow the transport of ions (typically protons) to complete the internal circuit in VRFBs [11,12]. Notwithstanding, the extensively used perfluorinated membranes (Nafion) possess most of the properties desired for VRFBs, their application has been limited by two issues: the severe migration issue of vanadium ions and the high cost [13,14]. On one hand, due to the particular structure of perfluorinated membranes, microphase separated and hydrated ionic aggregate clusters are well established. Normally, the microphase separation is beneficial for ionic migration. However, due to the large size of hydrophilic ionic clusters (4 nm–5 nm) [15], the ion selectivity of perfluorinated membranes is extremely low. That is, the vanadium ions with different oxidation states, which should be maintained in the separated electrolyte reservoirs, also migrate through the membrane accompanying the transport of protons as well as water molecules [16,17]. The severe migration of vanadium ions not only significantly reduces the utilization of electrolytes, but also causes a severe self-discharge process that decreases the energy efficiencies of the total flow battery system. On the other hand, the fabrication of perfluorinated membranes is complicated and time-consuming, leading to a high cost (500–700 dollar m^{-2}) [18]. More importantly, thick perfluorinated membranes are required for real applications to avoid the severe intermixing of vanadium ions. Based on the cost analysis made by Department of Energy (DOE) of America, the membrane cost was the main component of the total system cost (44% for 0.25 MWh and 27% for 4 MWh) [19,20].

To address these issues, alternative membranes, including hydrocarbon-based proton exchange membranes (PEMs) [21–23], anion exchange membranes (AEMs) [24–26] and nanofiltration membranes (NFs) [27,28], have been gradually applied in VRFBs. Among these membranes, AEMs have received considerable attention for application in VRFBs due to their low vanadium permeability, which results from the Donnan exclusion effect among the positively charged functional groups and vanadium ions [29–31]. Though attractive, AEMs are plagued by low chemical stability of functional groups in harsh acid environments. AEMs with traditional quaternary ammonium groups have been applied in VRFBs. However, the quaternary ammonium groups were demonstrated to be easily degraded in the harsh environments (high concentration of supporting electrolyte (H_2SO_4) and high oxidative reactive species (VO_2^+)) [31–33]. Recently, AEMs containing pyridinium groups have been applied in VRFBs owing to their promotion of proton transport due to acid-base interactions and their extended cycling life in VRFBs [34–36]. Moreover, an internal cross-linking network, created by reacting 4, 4′-bipyridine with the halomethyl on the modified polymer backbone, provided the AEMs with enhanced stability [14]. Nevertheless, subsequent research work demonstrated that the pyridinium groups still suffered severe degradation due to the introduction of hydrophilic carbon in the benzene ring during the course of the grafting process [37]. The induced hydrophilic carbon center was attacked by the long pair electron of VO_2^+, which caused not only the deterioration of the mechanical properties, but also the high internal resistance of VRFBs.

Herein, in the present work, we report a novel and durable AEM for VRFBs. Contrary to the backbone structure containing the electron-donating alkyl groups, we chose bromomethylated poly (2,6-dimethyl-1,4-phenylene oxide) (BrPPO) as the starting polymer to graft the pyridinium functional groups. More importantly, the bromomethyl groups can be cross-linked by the bipyridine during the course of thermal treatment. Hence, the chemical stability was improved that was ascribed to the internal cross-linking networks and the chemical inertness of polymer backbone. In addition, the bromomethylation process, which avoided the usage of the highly toxic and carcinogenic reagents (chloromethylether and trimethylamine), was more environmentally friendly. After the fabrication, we then evaluated the cell performance of the VRFBs assembled with the BrPPO/Py membranes and compared to the battery with perfluorinated membranes (Nafion 212). It was demonstrated that VRFBs with BrPPO/Py exhibited superior cell performance and excellent cycling stability. These results confirm that the BrPPO/Py membranes are the promising AEMs for redox flow batteries.

2. Experimental

2.1. Materials

1,2-bis(4-pyridyl)ethane (BisPE), *N*-bromosuccinimide (NBS), 2,2′-Azo-bis-isobutyronitrile (AIBN), dimethylformamide (DMF) and sulfuric acid (95 wt%) were purchased from Sigma-Aldrich. Poly(2,6-dimethyl-1,4-phenylene oxide) (PPO) with a molecular weight of 350,000 g mol^{-1} was obtained from SABIC Innovative Plastics (PPO6130). A Nylon membrane (pore size: 0.22 μm; OSMONICS Inc.) was used for the filtration process. ELAT® hydrophilic plain cloths and vanadyl sulfate ($VOSO_4 \cdot 3H_2O$, ≥99%) were purchased from FuelCellsEtc and Shenyang Haizhongtian Fine Chemical Factory, respectively. AIBN was twice recrystallized from methanol. All other chemicals were used as received without any further purification. Deionized (DI) water with resistivity not less than 18.2 MΩ (Millipore) was prepared for all aqueous solutions.

2.2. Synthesis of BrPPO/Py

The preparation process of the bromomethylated PPO (BrPPO) with different degrees of bromomethylation (DOB, ***x***) was achieved by controlling the ratio between the PPO and NBS, as reported elsewhere [38,39]. Generally, PPO (40 mmol) was dissolved in 200 mL chlorobenzene at 50 °C to obtain a light yellow solution. The solution was then added into a three-neck flask equipped with a water-cooling condenser and heated in an oil bath at 145 °C while magnetically stirred. The reaction was held at this temperature for 24 h after a desired mole of NBS and 4 mmol AIBN were successively added. Once the reaction was complete, the mixture was cooled down to room temperature. The resulting deep red solution was poured slowly into 1000 mL methanol to precipitate the brown polymer. The polymer was then filtrated, carefully rinsed with methanol several times, and subsequently dissolved in chloroform and re-precipitated in the hot methanol solution. The polymer was then dried overnight in a vacuum oven at 80 °C.

The as-prepared BrPPO was dissolved into DMF to form a 5 wt% solution. A predetermined amount of BisPE was then added. The mixture was stirred at room temperature for 12 h. The polymer solution was subsequently cast on a clean glass plate using a micrometer adjustable film applicator. The plate was then placed inside a forced convection oven. To completely evaporate the solvents, the oven temperature was maintained at 100 °C for 12 h and

subsequently cooled down to room temperature. The membranes were then immersed in DI water and peeled off the glass plate. The as-prepared BrPPO/Py membranes were denoted as BrPPO/Py-x, in which x represented the DOBs of the membranes.

2.3. Material structure characterizations

^{1}H NMR spectra were recorded on a high resolution NMR spectrometer (Varian Mercury, 300 MHz) at room temperature, using $CDCl_3$ as the solvent. Fourier transform infrared spectroscopy (FTIR) measurements were recorded using a Vertex 70 Hyperion 1000 (Bruker) with the assistance of attenuated total reflectance (ATR) accessories. The absorption spectra were recorded from 4000 cm^{-1} to 400 cm^{-1} with a resolution of 4 cm^{-1}. A field emission scanning electron microscope (FESEM, JEOL 7100) was used to determine the morphology of the membrane surface and cross-section with an acceleration voltage of 5 kV. Before FESEM observation, the membrane samples were fractured with liquid nitrogen and coated with gold.

The microstructures of BrPPO/Py were observed by high resolution transmission electron microscopy (HRTEM). The membrane samples were firstly dissolved in DMF to form a diluted solution (0.2 wt%) and cast on copper grids (400 mesh). After drying the solvent using an infrared lamp, the membrane samples were stained with periodic acid by placing the copper grids on the evaporating aqueous solution containing the periodic acid. TEM images were taken on a HRTEM (JEOL, 2010F TEM) using an accelerating voltage of 200 kV.

2.4. Water uptake measurement

The membrane samples were immersed in DI water, 3 M H_2SO_4 and 1 M V(IV)/V(III) (state of charge: 50%) +3 M H_2SO_4, respectively. The acid/vanadium doping process lasted for 5 days at 40 °C to ensure that the doping process was complete. Subsequently, the wet weight (m_{wet}) of the membranes was then measured at room temperature after the excess acid/vanadium solutions on the surface of BrPPO/Py were quickly wiped off with tissue paper. The membrane samples were then dried at 110 °C for 2 h in an oven and quickly weighed in a closed vessel (m_{dry1}). The membrane samples were then treated in DI water at 90 °C for 2 h to remove the residual acid/vanadium and dried at 110 °C for 2 h in an oven and quickly weighed in a closed vessel (m_{dry2}). During the weight measurement, membrane samples were periodically weighed until a constant value was obtained. Accordingly, water uptake (WU) was determined by:

$$WU = \frac{m_{wet} - m_{dry1}}{m_{dry2}} \times 100\% \quad (1)$$

2.5. Ionic conductivity and vanadium permeability measurements

Before the conductivity measurement, the as-prepared membranes were immersed into 3 M $MgSO_4$ for 48 h for the ionic exchange. The ionic conductivity of the membranes was determined with a potentiostat (Princeton Applied Research, PARSTAT M2273) through a two electrode conductivity clamp using an AC impedance method. The membrane samples were sandwiched by a pair of Au-coated stainless steel electrodes. The electrodes were then sandwiched between two PTFE plates and placed in a home-made container filled with DI water. To measure the ionic conductivity of the membrane in the acid solution and electrolyte, the membrane samples were firstly immersed into the acid solution (3 M H_2SO_4) and electrolyte (1 M $VOSO_4$ + 3 M H_2SO_4), respectively. The internal resistance was then measured with an in-house dialysis cell using platinum mesh as the current collector. A frequency range from 100 kHz to 1 Hz with a wave amplitude of 10 mV was applied to the conductivity clamp to obtain the AC impedance spectra. The membrane resistance (R_Ω) was obtained by calculating the intercept of the high frequency region. All the membrane resistances were measured three times. The ionic conductivity σ was obtained from:

$$\sigma = \frac{L}{R_\Omega \times A} \quad (2)$$

where L represents the thickness of the membrane (cm) and A represents the surface area of the membrane (cm^2).

The permeability of VO^{2+} through the BrPPO/Py membrane was determined by an in-house dialysis cell according to our previous report [40]. The membrane was tightly sandwiched between two chambers with the same volume (50 mL). Chamber A was filled with 1.0 M $VOSO_4$ + 3 M H_2SO_4 while Chamber B was filled with 1.0 M $MgSO_4$ + 3 M H_2SO_4. The $MgSO_4$ was added to balance the ionic strengths of the two solutions and to minimize the osmotic pressure effects between the two sides of the membranes. Magnetic stirrers were used in both cells to avoid concentration polarization. Solution samples from Chamber B (1 mL) were collected at regular time intervals and analyzed for vanadium ion concentration by inductively coupled plasma mass spectrometry (ICP-MS). 1 mL of pristine solution (1.0 M $MgSO_4$ + 3 M H_2SO_4) was immediately added to Chamber B after sampling to maintain a constant solution volume. The vanadium permeability of the membrane was calculated by the following equation:

$$V\frac{dc_t}{dt} = A\frac{P}{L}(c_0 - c_t) \quad (3)$$

where, V is the volume of solution in both chambers (50 cm^3), A the membrane area exposed to the solution (cm^2), P the permeability of vanadium ions (cm^2 s^{-1}), L the thickness of the membrane (cm), c_0 and c_t the initial vanadium concentration (mol cm^{-3}) and the vanadium concentration in Chamber B at time t (s), respectively.

After obtain the ionic conductivities and permeabilities for BrPPO/Py, we introduced the selectivity to quantify the relationship, as reported elsewhere [41]:

$$\alpha_{V4} = \frac{\kappa RT}{F^2 P_{V4} c_{V4}} \quad (4)$$

where α_{V4} is the dimensionless selectivity for VO^{2+}, κ is the conductivity in S m^{-1}, R is the universal gas constant in J mol^{-1} K^{-1}, T is the absolution temperature in K, F is the Faraday constant in C mol^{-1}, P_{V4} is the permeability of VO^{2+} in m^2 s^{-1}, and c_{V4} is the concentration of VO^{2+} in the solution adjacent to the membrane (mol m^{-3}).

2.6. Chemical stability test

The *ex-situ* chemical stability test was performed according to the previous procedure as reported elsewhere [42,43]. The membranes were cut to a size of 30 mm × 30 mm and separately submerged in 20 mL of 0.1 M V(V) in 5.0 M total sulfate. The 0.1 M V(V) + 5 M H_2SO_4 was prepared by diluting the 1 M V(V) + 5 M H_2SO_4 with concentrated sulfuric acid (95 wt%). The 1 M V(V) + 5 M H_2SO_4 was prepared by electrochemically oxidizing the solution of 1 M $VOSO_4$ + 5 M H_2SO_4 with a current density of 20 mA cm^{-2} in a flow cell. The electrolyte solution containing the

as-prepared membranes was sealed and placed at ambient temperature or in a silicone oil bath (40 °C). Nafion 212 samples with the same size were also separately submerged in the same solutions for the purpose of comparison. Solution samples with the generated V(IV) ions were collected at regular time intervals and analyzed for the concentration of V(IV) by an ultraviolet visible spectrophotometer (Perkin Elmer, Model Lambda 20). A blank solution without the membranes was collected at regular time intervals and analyzed as reference for all the measurements. The absorbance of each mixture was determined at a wavelength number of 764 nm. Meanwhile, the membrane weight was also determined at regular time intervals. The FTIR spectra of the membrane after the measurements were determined when the doped acid and VO_2^+ were removed from the membranes.

2.7. VRFB single cell performance characterization

The cell performance of the VRFBs was measured with the setup of flow cells, as described in our previous work [44]. The flow cells with a flow by mode consisted of two aluminium end-plates, two gold-coated copper current collectors, two graphite-plate electrodes, and two polytetrafluorethylene (PTFE) gaskets. A serpentine flow field (1.0 mm in width, 1.5 mm in depth, and 1.0 mm in rib width) with an area of 2 cm × 2 cm was machined on one side of the graphite plates. ELAT® hydrophilic plain cloths with an uncompressed thickness of 406 μm were employed as the positive and negative electrode. Before cell assembling, the plain carbon cloths were activated by KOH at 800 °C for 30 min under a nitrogen atmosphere and then annealed at 400 °C for 6 h in ambient air to improve the electrochemical activity and hydrophilic property. Three pieces of plain cloth were employed on each side. The electrode compression ratio was 41.6%. Before assembling the battery, the membranes, including the fabricated BrPPO/Py and Nafion 212, were immersed in 3 M H_2SO_4 for 24 h.

The single cell was connected to two reservoirs containing 25 mL of 1 M V(IV) + 3 M H_2SO_4 and 25 mL of 1 M V(III) + 3 M H_2SO_4 in the positive side and negative side, respectively. Electrolytes were supplied by a peristaltic pump (WT600-2J, Longer pump) with a flow rate of 46 mL min^{-1} (60 rpm). The positive electrolyte was simply prepared by dissolving vanadyl sulfate powder in the sulfuric acid solution, while the negative electrolyte was freshly prepared by electrochemically reducing the solution of 1 M $VOSO_4$ + 3 M H_2SO_4 into 1 M V(III) + 3 M H_2SO_4 with a current density of 20 mA cm^{-2} in an electrolyzer equipped with platinized titanium mesh electrodes. The two reservoirs were both purged with nitrogen gas (high-purity) and then sealed prior to the electrochemical tests to minimize oxidation of the active species. The performance of the VRFBs was measured using a potentiostat/galvanostat (Arbin Instrument) to provide a constant-current. All measurements were performed at room temperature (25 °C). The cut-off voltages for charge and discharge were 1.7 V and 0.9 V, respectively. The capacity (Ah) and energy (Wh) during the discharge and charge process were recorded by Arbin and the coulombic efficiency (CE) and energy efficiency (EE) were obtained from:

$$CE = \frac{\text{Discharge capacity}}{\text{Charge capacity}} \times 100\% \quad (5)$$

$$EE = \frac{\text{Discharge energy}}{\text{Charge energy}} \times 100\% \quad (6)$$

The voltage efficiency (VE) was obtained by:

$$VE = \frac{EE}{CE} \times 100\% \quad (7)$$

3. Results and discussion

3.1. Characterization of BrPPO/Py

The BrPPO/Py was fabricated by a facile synthesis route, including the bromomethylation process of PPO and the grafting process of pyridinium groups [39,45]. BrPPO with different degrees of bromomethylation (DOB) was prepared, as presented in Fig. 2a. With the increased DOB, more bromomethyl groups were grafted on the skeleton of PPO, and thereby the portion of grafted pyridinium functional groups was also increased. Thereafter, the BrPPO/Py membranes were prepared by reacting the as-prepared BrPPO with BisPE at room temperature. After that, BrPPO/Py was fabricated by a solution-cast method and a thermal treatment thereafter. In the course of the thermal treatment, the membrane was internally cross-linked through the pyridinium groups (Fig. 1). The chemical structure of the final BrPPO/G was characterized by FTIR, as shown in Fig. 2b. After the cross-linking process, the peak at 1510 cm^{-1} emerges in the FTIR spectrum of BrPPO/Py-56, indicating that pyridinium functional groups were successfully grafted on the BrPPO backbones due to these characteristic peaks are attributed to the stretching vibrations of the pyridine C=N bond [14].

Due to the formation of gel for BrPPO/Py-82, the cross-linked BrPPO/Py membranes with three relatively low DOBs were prepared. The BrPPO/Py membranes are light-yellow, dense and flexible membranes with a rough thickness of 50 μm, as shown in Fig. 3a. The microscopic morphologies of the cross-linked BrPPO/Py were determined by SEM and HRTEM. As shown in Fig. 3b–c, it is clearly observed that a uniform, dense and smooth membrane without the existence of any pores in the surface and cross-section review is formed. The BrPPO/Py membranes were then stained with periodic acid and characterized by HRTEM, as shown in Fig. 3d. The dark regions correspond to the hydrophilic pyridinium functional groups due to their affinity with IO_4^- anions, while the bright regions correspond to the hydrophobic aromatic polymer backbones. The hydrophilic regions with an average size of 2.3 (±0.2) nm were uniformly distributed throughout the entire measured area, indicating that a nano-phase separation of hydrophilic/hydrophobic microstructure was uniformly established in the BrPPO/Py membranes.

3.2. Ionic conductivity and vanadium permeability

To assess the ionic conductivity of BrPPO/Py, the membranes were immersed in different solutions for 24 h before the conductivity measurement. As presented in Fig. 4a, the ionic conductivity of BrPPO/Py significantly increases with an increase in DOB although the ionic conductivities of BrPPO/Py are lower than those of Nafion 212. In DI water, BrPPO/Py-70 possessess a through-plane ionic conductivity of 8.8 mS cm^{-1} at room temperature, in comparison to 39.5 mS cm^{-1} for Nafion 212. Due to the electrolyte of VRFBs is a multi-ion environment, which includes the vanadium ions, protons, sulfate ions. The ionic conductivity of the membrane was affected by the uptake of electrolytes in the real battery system [46]. We believe that both the proton and sulfate ions contribute to ionic conductivity. Hence, the ionic conductivity can be described as:

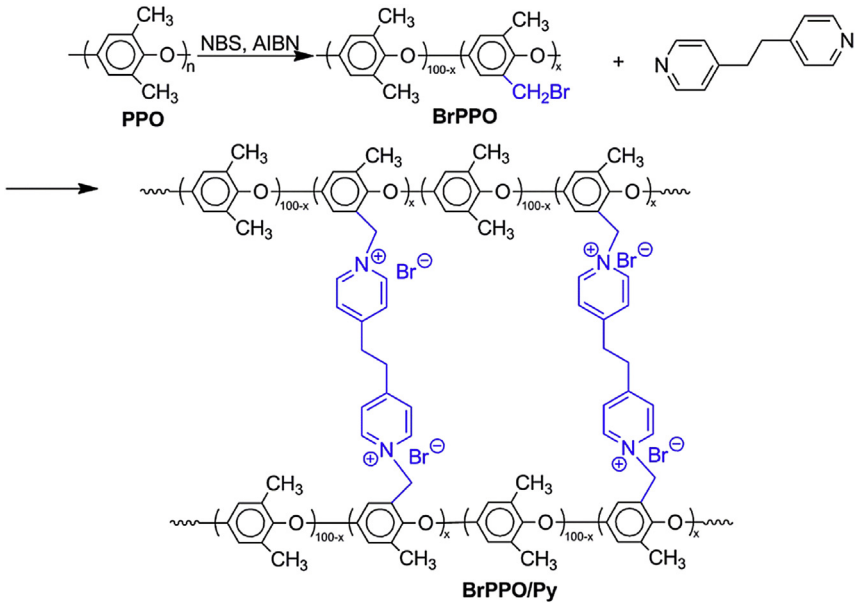

Fig. 1. Scheme of the synthesis route of pyridinium-functionalized BrPPO (BrPPO/Py).

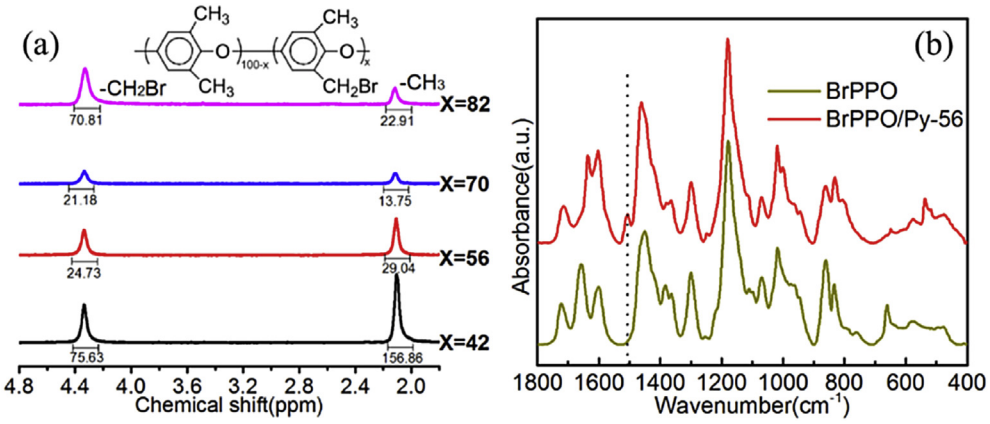

Fig. 2. (a) ^{1}H NMR spectra of BrPPO in $CDCl_3$; (b) ATR-FTIR spectra of BrPPO and BrPPO/Py-56. The chemical structure of BrPPO is also included in the panel (a).

$$\sigma = \sigma_{H^+} + \sigma_{SO_4^{2-}} \quad (8)$$

where the σ is the total ionic conductivity. σ_{H^+} and $\sigma_{SO_4^{2-}}$ are the conductivity contributed by protons and the imbibed sulfate ions in the membranes, respectively. In cation exchange membranes (Nafion), the predominant conducting ions are protons, while both the sulfate ions and protons contribute to the total ionic conductivity in anion exchange membranes with the existence of uptaken electrolytes [25]. This is due to the fact that the AEMs are saturated with the liquid electrolyte (H_2SO_4). Meanwhile, the ionic mobility of the protons is more than three times higher than that of the sulfate ions (36.23×10^{-8} m^2 V^{-1} s^{-1} *vs.* 8.29×10^{-8} m^2 V^{-1} s^{-1}) [47]. Therefore, the protons resulting from the ionization of the imbibed liquid electrolyte should also be transported in the BrPPO/Py membrane. For example, after being treated in 3 M H_2SO_4, BrPPO/Py-70 possesses an ionic conductivity of 33.9 mS cm^{-1} at room temperature. The augmented conductivity results from the sulfuric acid dissociation, which enables production of a large number of extra protons and contributes to the ionic conductivity. Nafion 212 also has a similar phenomenon. However, when the membranes were immersed in 1 M V^{3+}/V^{4+} (state of charge: 50%) + 3 M H_2SO_4, the ionic conductivities declined to some extent. This is caused by the vanadium uptake in these membranes. It should be noted that the reduced ratio for BrPPO/Py is lower than that of Nafion 212, which is caused by the high vanadium uptake in Nafion 212. It should be also noted that we used the ionic mobilities of protons and sulfate ions in the liquid phase for a simple comparision. In fact, the imbibed sulfuric acid can increase the proton and sulfate ion concentration in the membrane, but significantly reduce the ion mobility by reducing the water content [48].

To clarify the promotion of the ionic conductivity by the imbibed liquid electrolyte, we measured the water uptake of BrPPO/Py in three types of solutions and compared this with Nafion 212, as presented in Fig. 4b. The water uptakes of BrPPO/Py are lower than those of Nafion 212 in DI water, which is a result of the different microstructures as proven by HRTEM. However, the water uptake of Nafion 212 in 3 M H_2SO_4 is significantly reduced. The reduction in water uptake in 3 M H_2SO_4 also occurs in the BrPPO/Py membranes in spite of the fact that the reduction ratio is low. The results demonstrate that the conductivity enhancement in these membranes is ascribed to the imbibed liquid electrolyte. Meanwhile, the

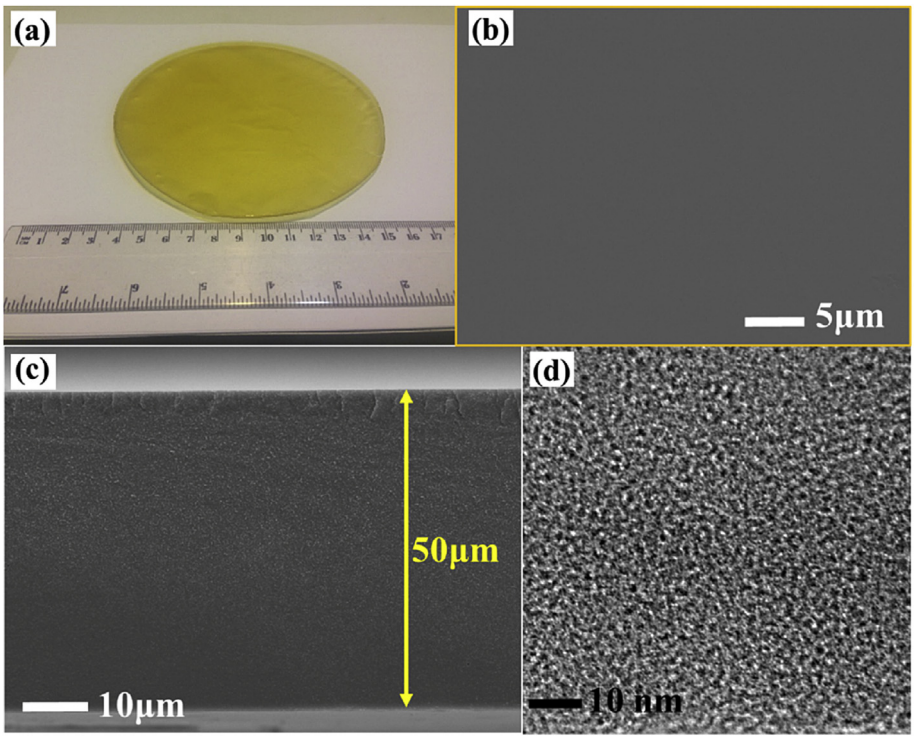

Fig. 3. (a) Digital photograph of BrPPO/Py-56; a typical surface morphology (b) and cross-section morphology (c) of BrPPO/Py-56; (d) HRTEM image of BrPPO/Py-56.

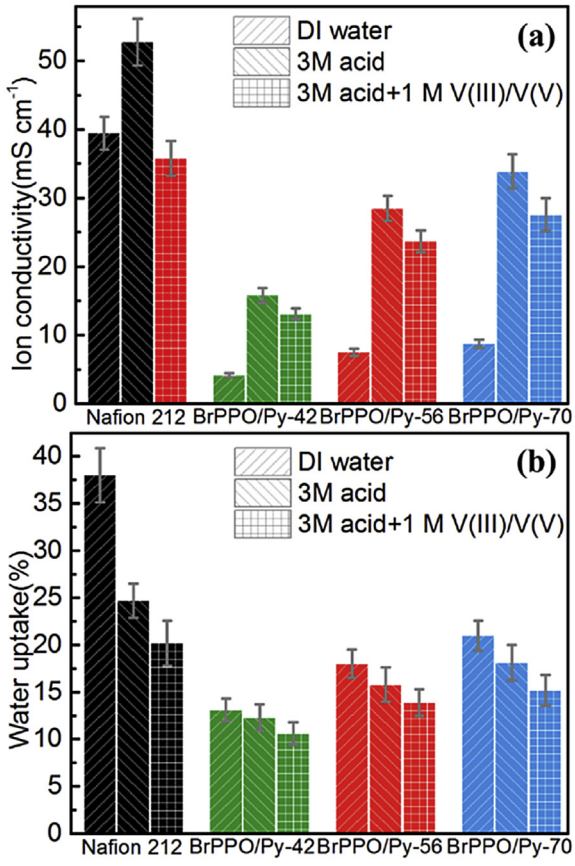

Fig. 4. Ion conductivity (a) and water uptake (b) of BrPPO/Py and Nafion 212 under different solutions.

water uptake in Nafion 212 is further reduced in 1 M V(IV)/V(III) with 3 M H_2SO_4 in accompany with the imbibed vanadium ions. The sulfonic acid groups have a stronger electrostatic attraction with the vanadium ions because the vanadium ions have a relatively higher chemical state than the monovalent protons. Also, it should be noted that the reduction of water uptake for BrPPO/Py in 1 M V(IV)/V(III) with 3 M H_2SO_4 is lower due to the fact the vanadium ions with positive charge can be effectively kept out of BrPPO/Py, which is referred to as the Donnan exclusion effect. Therefore, the membrane dehydration caused by the uptake of vanadium is relatively low.

The vanadium permeability through the BrPPO/Py membranes was then measured and compared with Nafion 212. As shown in Fig. 5a, it is obvious that the concentrations of V(IV) permeating the BrPPO/Py membranes are remarkably lower than those of V(IV) permeating Nafion 212. By linearly fitting the concentration versus diffusion time, the permeability of V(IV) can be obtained from the fitted slope. As presented in Fig. 5b, Nafion 212 exhibits a permeability of 7.54×10^{-7} cm^2 min^{-1}, which is comparable to or even lower than the results reported in the literature [22,41,49]. It is demonstrated that the permeabilities for all the BrPPO/Py membranes are significantly lower than that of Nafion 212. BrPPO/Py-70 possesses a maximum permeability of 0.36×10^{-7} cm^2 min^{-1}, which is still much lower than that of Nafion 212. The dimensionless selectivity defined as the ionic conductivity over vanadium permeability was calculated based on Eq. (4). As exhibited in Fig. 5c, the selectivity of BrPPO/Py-56 (16,181.1) is twenty times higher than that of Nafion 212 (758.9). Even the BrPPO/Py-70, which exhibits the highest permeability, possesses a selectivity of 12,316.9, which is still fifteen times higher than that of Nafion 212. The extremely high selectivity is attributed to the following two reasons. First, the pyridinium functional groups effectively reduce the transmembrane migration of vanadium ions due to the Donnan exclusion effect between the positive functional groups and the hydrated vanadium ions. Secondly, the sizes of well-established

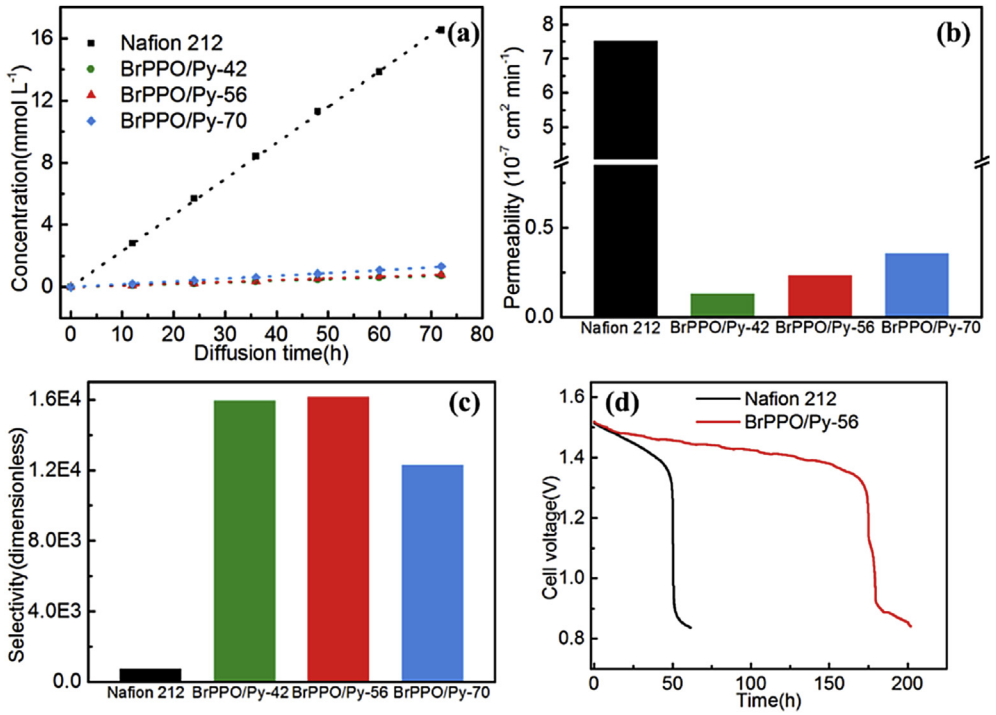

Fig. 5. (a) Concentration change of VO^{2+} ions in the $MgSO_4$ chamber across BrPPO/Py and Nafion 212; A comparison of VO^{2+} ions permeability (b) and selectivity (c) of BrPPO/Py and Nafion 212. (d) Open circuit voltage decay of fully charged VRFBs with BrPPO/Py-56 and Nafion 212.

hydrophilic regions in the BrPPO/Py membranes are smaller than those of the perfluorinated membranes [50]. The small ionic clusters will dramatically hinder the migration of vanadium ions. It should be noted that the permeabilities through the BrPPO/Py membranes increase with an increase in the DOBs. With the increased DOB, more pyridinium functional groups were grafted on the backbone of BrPPO, therefore the Donnan exclusion effect should be increased. However, the volume ratio of hydrophilic domains in BrPPO/Py-70 was also increased, which led to a reduction of selectivity for BrPPO/Py-72. Nevertheless, the result demonstrates that the BrPPO/Py membranes exhibit an impressive suppression effect on the vanadium ion permeability.

To confirm the superior selectivity of BrPPO/Py, a self-discharge test of fully charged VRFBs assembled with BrPPO/Py-56 and Nafion 212 was also performed (Fig. 5d). As a result of the gradual migration of vanadium ions across the membranes, the open circuit voltage (OCV) slightly descends at first and then rapidly drops to around 0.8 V. For the VRFB with BrPPO/Py-56, the maintaining time of OCV above 0.8 V is 202 h, which is 2.3-fold longer than that of the VRFB with Nafion 212 (61 h). The severe decay of OCV for Nafion 212 compared with BrPPO/Py-56 further demonstrates that the migration of vanadium ions across BrPPO/Py-56 is greatly reduced, which is in good accordance with the individual diffusion cell test.

3.3. Chemical stability

The chemical stability is also a crucial requirement for membranes applied in VRFBs due to the harsh chemical environments (high concentration of supporting electrolyte (H_2SO_4) and high oxidative reactive species (VO_2^+)). The chemical stability was determined by an *ex-situ* immersion test, as reported elsewhere [51,52]. As shown in Fig. 6a, BrPPO/Py-56 became dark-yellow and crimped with a reduced dimension after the durability test, regardless of the treatment temperature. Although BrPPO/Py-56 became brittle at 40 °C after the durability test, an integrated membrane structure is still maintained. The immersed electrolyte (0.1 M V(V) + 5 M H_2SO_4) became light-green at room temperature, as exhibited in Fig. 6b. While the immersed electrolyte became dark-green at the elevated temperature, owing to the generation of VO^{2+} derived from the membrane degradation. The generated VO^{2+} concentration was then quantified by a UV–Vis spectrophotometer. As shown in Fig. 6c, the generated VO^{2+} concentration derived from the oxidation of polymer in BrPPO/Py-56 slightly increases with the increased immersion time at room temperature. Although BrPPO/Py-56 possesses a higher generation rate of VO^{2+} than Nafion 212, the generation rates are relatively lower than the results reported in the literature [37,53]. The superior chemical stability should be attributed to the following two reasons. Firstly, there exists the Donnan exclusion effect, which limited the oxidative V(V) ions permeating into the membrane. This can be proved by the low vanadium uptake measured in Section 3.2. Secondly, the internal cross-linking networks are well established, therefore the free volume of the membrane is reduced, which will effectively resist the oxidative V(V) ions attacking the membrane.

However, when the temperature is elevated to 40 °C, the V(IV) concentration in BrPPO/Py-56 is four times greater than that of BrPPO/Py-56 at ambient temperature after 20 days, indicating that the elevated temperature accelerates the degradation of BrPPO/Py-56. The severe degradation can also be observed by the weight loss of the membrane samples, as presented in Fig. 6d. The weight loss for BrPPO/Py-56 is about 30 wt% after 20 days. The FTIR spectra of BrPPO/Py-56 before and after the *ex situ* immersion test were measured to analyze the degradation mechanism (Fig. 6e). The peak at 1510 cm^{-1} still exists in the FTIR spectrum of BrPPO/Py-56 after the *ex situ* immersion test in spite of the reduction of peak strength. This result indicates that partial pyridinium groups survive in the harsh environment. Meanwhile, a new characteristic peak emerging at about 1390 cm^{-1}, which should be assigned to −OH plane bending of a motion of hydroxyl groups derived from the degradation of the membrane samples. The absorption bands at

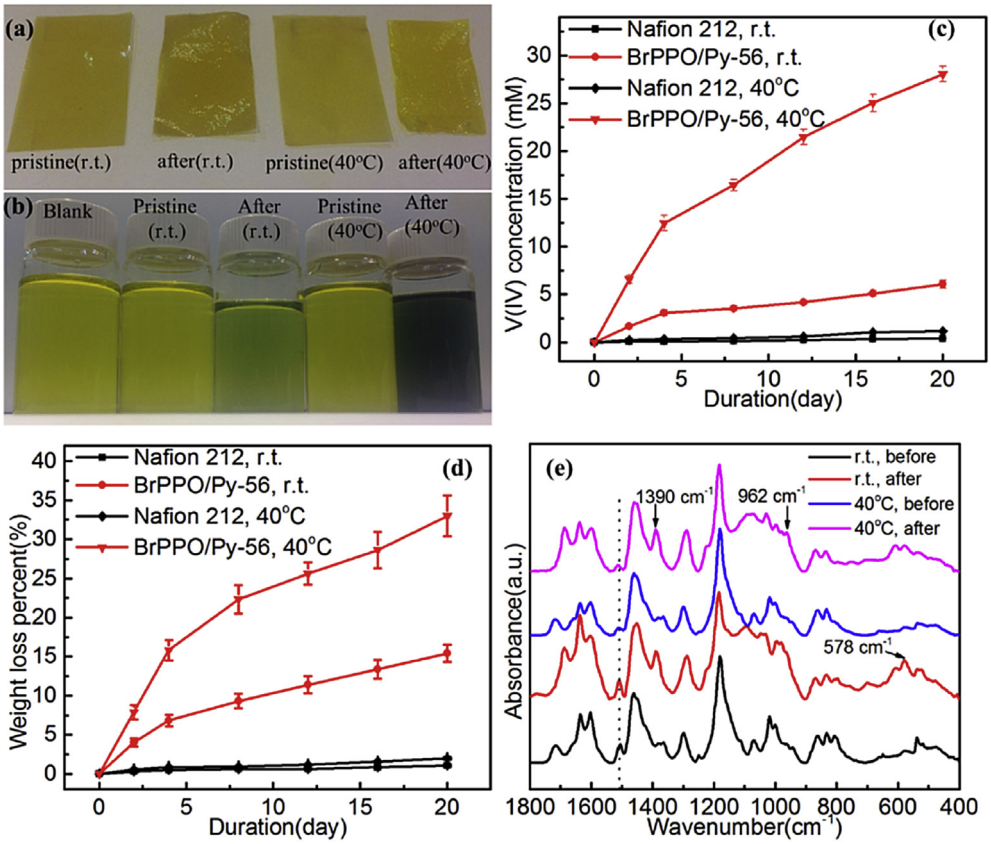

Fig. 6. Digital photographs of BrPPO/Py-56 (a) and the electrolyte solution (b) after the durability test (20 days); (c) VO^{2+} concentration of solutions containing BrPPO/Py-56 and Nafion 212 in different conditions; (d) The weight loss percentage of BrPPO/Py-56 and Nafion 212 in different conditions; (e) FTIR spectra of BrPPO/Py-56 measured at different conditions during the durability test. The deviations for the data presented in pane (c) and (d) were calculated based on three individual measurements.

about 962 cm^{-1} and 578 cm^{-1} existing in the degraded membrane are assigned to the absorbed vanadium oxygen species [37]. It can be concluded that the pyridinium groups in the BrPPO/Py membranes are partially oxidized by highly oxidative V(V) ions and converted to $-CH_2OH$ during the course of the durability test. The type of degradation will maintain the integration of the membrane as the polymer backbones are survived.

3.4. Cell performance

The cell performance was then evaluated in single-cell VRFBs respectively assembled with BrPPO/Py and Nafion 212 with the same thickness at room temperature under otherwise identical electrode preparations and operating conditions. The charge-discharge curves were measured with a constant-current mode when the current densities ranged from 100 mA cm^{-2} to 250 mA cm^{-2}. As exhibited in Fig. 7a, the discharge voltages of VRFBs with BrPPO/Py are lower than those of the batteries with Nafion 212 as a result of the low ionic conductivity of BrPPO/Py. However, the specific discharge capacities of VRFBs with BrPPO/Py are higher than those of the batteries with Nafion 212. The CEs and EEs were analyzed to evaluate the cell performance. As presented in Fig. 7b, the CEs of VRFBs with the BrPPO/Py membranes are higher than those of VRFBs with Nafion 212, which is indicative of the low vanadium transmembrane permeation through the BrPPO/Py membranes. With an increase in current density, the CEs of VRFBs increase monotonically, which results from the short charge/discharge time for vanadium crossover at a higher current density. It should be noted that the CEs for all the BrPPO/Py membranes are higher than 97% when the current density is higher than 100 mA cm^{-2}, which suggests that the possible side reactions related to the membrane are minimal.

As shown in Fig. 7c, an improvement in EEs is observed when the DOB increases from 42% to 56% and the EEs reduce to some extent when the DOB further increases to 70%. It is demonstrated that there is a trade-off between the ionic conductivity and vanadium permeability for the BrPPO/Py membranes. With a low DOB, VRFBs with BrPPO/Py-42 exhibits the highest CE with the lowest VE, which is caused by a large charge/discharge overpotential as a result of low ionic conductivity. While the VRFB with BrPPO/Py-70 shows the lowest CE with a relatively high EE, which is caused by the large vanadium transmembrane diffusion as a result of high permeability. It is noteworthy that the EE of VRFBs with BrPPO/Py-56 is 3.1% higher than that of battery with Nafion 212 at a current density of 100 mA cm^{-2}. With an increase in the applied current density, the discrepancy of EEs between BrPPO/Py-56 and Nafion 212 decreases, which indicates that a membrane with high ionic conductivity is highly required at a high current density. Nevertheless, the results shown here demonstrate BrPPO/Py-56 is a promising candidate for VRFBs, owing to the superior balance of ionic conductivity and vanadium permeability. Also, the VRFBs with BrPPO/Py exhibit a good charge-discharge rate capability as shown in Fig. 7d, in which the specific discharge capacities of VRFBs with BrPPO/Py at 250 mA cm^{-2} reduce to *ca.* 73% of the corresponding capacities of VRFBs with BrPPO/Py at 100 mA cm^{-2}. The decline in the capacity is caused by an increased charge/discharge overpotential caused by a fast charge/discharge rate.

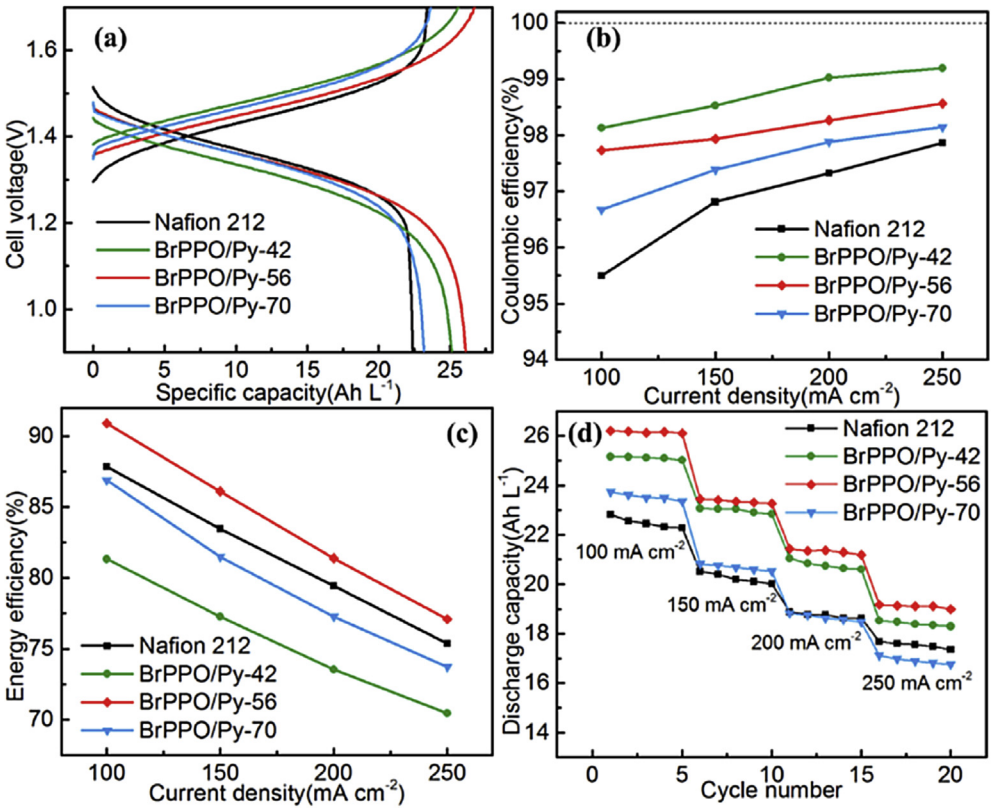

Fig. 7. (a) Charge-discharge curves of VRFBs with BrPPO/Py and Nafion 212 at 100 mA cm^{-2}; Coulombic efficiency (b) and energy efficiency (c) of VRFBs with BrPPO/Py and Nafion 212 at different current densities; Specific discharge capacity (d) of VRFBs as a function of cycle number at different current densities.

3.5. Cycling stability

The chemical stability of BrPPO/Py was then evaluated by a cycling test, in which VRFBs assembled with BrPPO/Py-56 were cycled at a current density of 200 mA cm^{-2}. It should be mentioned that there was no electrolyte rebalance in the cycling test. As illustrated in Fig. 8a, the specific discharge capacity of VRFBs with BrPPO/Py-56 decreased to 80% of the initial value in 537 cycles with a capacity decay rate of 0.037% $cycle^{-1}$. In comparison to VRFBs with Nafion 212, the specific discharge capacity decreased to 80% of the initial value in 302 cycles with a capacity decay rate of 0.067% $cycle^{-1}$. The cycling tests demonstrate that the battery with BrPPO/Py-56 shows a much higher capacity retention than the one with Nafion 212. Meanwhile, the CEs of VRFBs with BrPPO/Py-56 maintained above 97% during the cycling test despite the existence of fluctuation which was caused by the temperature fluctuation, as presented in Fig. 7b. The superior cycling performance is ascribed to the superior chemical stability and high ion selectivity, which enable the BrPPO/Py-56 membrane to bear the harsh environment and reduce the vanadium transmembrane migration, in good agreement with the *ex situ* permeability measurements and chemical stability measurements.

4. Conclusions

In summary, we have fabricated a cross-linked pyridinium-

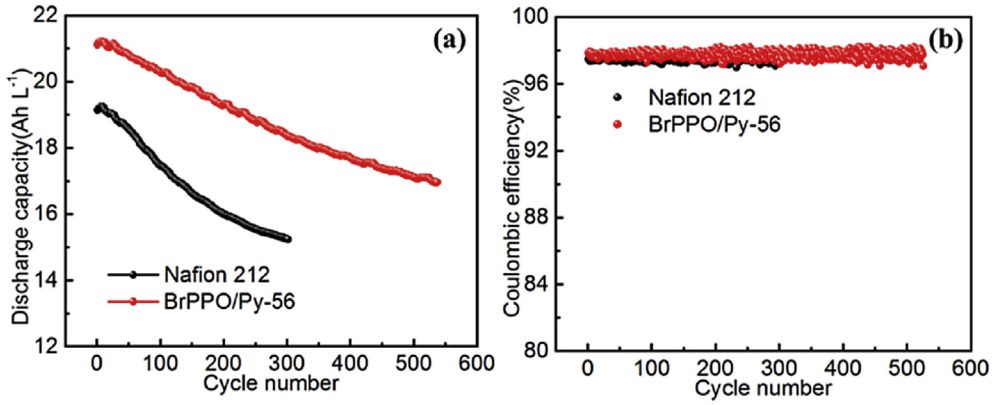

Fig. 8. Discharge capacity of VRFBs assembled with BrPPO/Py-56 and Nafion 212, respectively. The current density for charge and discharge is 200 mA cm^{-2}.

functionalized AEM to address the issue of low chemical stability for VRFBs. The as-prepared AEMs, namely BrPPO/Py, exhibited reasonably high conductivities and low vanadium permeabilities. At room temperature, BrPPO/Py-56 showed an ionic conductivity of 23.7 mS cm^{-1} and a vanadium permeability of 0.234×10^{-7} cm^2 min^{-1}, which was much lower than that of perfluorinated membranes (Nafion 212). The significant reduction in the transmembrane migration of vanadium ions through BrPPO/Py contributed to the Donnan exclusion effect and the well-established microstructures. More importantly, the BrPPO/Py membranes exhibited a superior chemical stability that was attributed, in part, to the internal cross-linking networks, and in part, to the fact that the polymer backbone was chemically inert. The superior chemical stability was not only demonstrated in the *ex situ* immersion test, but also verified in the continuous cycling test, in which the specific discharge capacity decreased to 80% of the initial value in 537 cycles with a capacity decay rate of 0.037% $cycle^{-1}$ at a current density of 200 mA cm^{-2}. Therefore, this work strongly demonstrates that the BrPPO/Py membranes are promising for redox flow batteries to achieve superior cell performance and excellent cycling stability.

Acknowledgements

The work described in this paper was fully supported by a grant from the Research Grants Council of the Hong Kong Special Administrative Region, China (Project No. 623313).

References

[1] W. Wang, Q. Luo, B. Li, X. Wei, L. Li, Z. Yang, Adv. Funct. Mater. 23 (2013) 970–986.
[2] G.L. Soloveichik, Chem. Rev. 115 (2015) 11533–11558.
[3] M. Skyllas-Kazacos, M.H. Chakrabarti, S.A. Hajimolana, F.S. Mjalli, M. Saleem, J. Electrochem. Soc. 158 (2011) R55–R79.
[4] J. Noack, N. Roznyatovskaya, T. Herr, P. Fischer, Angew. Chem. Int. Ed. 54 (2015) 9775–9808.
[5] Z. Yang, J. Zhang, M.C.W. Kintner-Meyer, X. Lu, D. Choi, J.P. Lemmon, J. Liu, Chem. Rev. 111 (2011) 3577–3613.
[6] B. Huskinson, M.P. Marshak, C. Suh, S. Er, M.R. Gerhardt, C.J. Galvin, X. Chen, A. Aspuru-Guzik, R.G. Gordon, M.J. Aziz, Nature 505 (2014) 195–198.
[7] K.X. Lin, Q. Chen, M.R. Gerhardt, L.C. Tong, S.B. Kim, L. Eisenach, A.W. Valle, D. Hardee, R.G. Gordon, M.J. Aziz, M.P. Marshak, Science 349 (2015) 1529–1532.
[8] A. Parasuraman, T.M. Lim, C. Menictas, M. Skyllas-Kazacos, Electrochim. Acta 101 (2013) 27–40.
[9] K.J. Kim, M.S. Park, Y.J. Kim, J.H. Kim, S.X. Dou, M. Skyllas-Kazacos, J. Mater. Chem. A 3 (2015) 16913–16933.
[10] Y.Y. Shao, Y.W. Cheng, W.T. Duan, W. Wang, Y.H. Lin, Y. Wang, J. Liu, ACS Catal. 5 (2015) 7288–7298.
[11] X. Li, H. Zhang, Z. Mai, H. Zhang, I. Vankelecom, Energy Environ. Sci. 4 (2011) 1147–1160.
[12] B. Schwenzer, J. Zhang, S. Kim, L. Li, J. Liu, Z. Yang, Chemsuschem 4 (2011) 1388–1406.
[13] E.M. Davis, J. Kim, V.P. Oleshko, K.A. Page, C.L. Soles, Adv. Funct. Mater. 25 (2015) 4064–4075.
[14] W.X. Xu, Y.Y. Zhao, Z.Z. Yuan, X.F. Li, H.M. Zhang, I.F.J. Vankelecom, Adv. Funct. Mater. 25 (2015) 2583–2589.
[15] K.A. Mauritz, R.B. Moore, Chem. Rev. 104 (2004) 4535–4585.
[16] S.A. Zhang, J.C. Li, X.D. Huang, Y.P. Zhang, Y.D. Zhang, Polym. J. 47 (2015) 701–708.
[17] H. Zhang, H. Zhang, X. Li, Z. Mai, W. Wei, Y. Li, J. Power Sources 217 (2012) 309–315.
[18] Y.Y. Zhao, M.R. Li, Z.Z. Yuan, X.F. Li, H.M. Zhang, I.F.J. Vankelecom, Adv. Funct. Mater. 26 (2016) 210–218.
[19] V. Viswanathan, A. Crawford, L. Thaller, D. Stephenson, S. Kim, W. Wang, G. Coffey, P. Balducci, Z. Gary Yang, L. Li, USDOE-OE ESS Peer Review at Washington, DC, 2012.
[20] B.R. Chalamala, T. Soundappan, G.R. Fisher, M.R. Anstey, V.V. Viswanathan, M.L. Perry, Proc. IEEE 102 (2014) 976–999.
[21] Z. Li, W. Dai, L. Yu, L. Liu, J. Xi, X. Qiu, L. Chen, ACS Appl. Mater. Interfaces 6 (2014) 18885–18893.
[22] X. Ling, C. Jia, J. Liu, C. Yan, J. Membr. Sci. 415 (2012) 306–312.
[23] C. Fujimoto, S. Kim, R. Stains, X. Wei, L. Li, Z.G. Yang, Electrochem. Commun. 20 (2012) 48–51.
[24] S. Yun, J. Parrondo, V. Ramani, Chempluschem 80 (2015) 412–421.
[25] D. Chen, M.A. Hickner, E. Agar, E.C. Kumbur, Electrochem. Commun. 26 (2013) 37–40.
[26] F. Zhang, H. Zhang, C. Qu, Chemsuschem 6 (2013) 2290–2298.
[27] H. Zhang, H. Zhang, X. Li, Z. Mai, J. Zhang, Energy Environ. Sci. 4 (2011) 1676–1679.
[28] H. Zhang, H. Zhang, X. Li, Z. Mai, W. Wei, Energy Environ. Sci. 5 (2012) 6299–6303.
[29] S. Zhang, B. Zhang, G. Zhao, X. Jian, J. Mater. Chem. A 2 (2014) 3083–3091.
[30] S.-J. Seo, B.-C. Kim, K.-W. Sung, J. Shim, J.-D. Jeon, K.-H. Shin, S.-H. Shin, S.-H. Yun, J.-Y. Lee, S.-H. Moon, J. Membr. Sci. 428 (2013) 17–23.
[31] Z. Mai, H. Zhang, H. Zhang, W. Xu, W. Wei, H. Na, X. Li, Chemsuschem 6 (2013) 328–335.
[32] C.N. Sun, Z.J. Tang, C. Belcher, T.A. Zawodzinski, C. Fujimoto, Electrochem. Commun. 43 (2014) 63–66.
[33] S. Zhang, C. Yin, D. Xing, D. Yang, X. Jian, J. Membr. Sci. 363 (2010) 243–249.
[34] B. Zhang, E. Zhang, G. Wang, P. Yu, Q. Zhao, F. Yao, J. Power Sources 282 (2015) 328–334.
[35] S. Maurya, S.H. Shin, K.W. Sung, S.H. Moon, J. Power Sources 255 (2014) 325–334.
[36] H. Zhang, H. Zhang, F. Zhang, X. Li, Y. Li, I. Vankelecom, Energy Environ. Sci. 6 (2013) 776–781.
[37] Z.Z. Yuan, X.F. Li, Y.Y. Zhao, H.M. Zhang, ACS Appl. Mater. Interfaces 7 (2015) 19446–19454.
[38] A. Katzfuss, V. Gogel, L. Jorissen, J. Kerres, J. Membr. Sci. 425 (2013) 131–140.
[39] L. Zeng, T.S. Zhao, J. Power Sources 303 (2016) 354–362.
[40] P.K. Leung, Q. Xu, T.S. Zhao, L. Zeng, C. Zhang, Electrochim. Acta 105 (2013) 584–592.
[41] W. Xie, R.M. Darling, M.L. Perry, J. Electrochem. Soc. 163 (2016) A5084–A5089.
[42] S. Winardi, S.C. Raghu, M.O. Oo, Q. Yan, N. Wai, T.M. Lim, M. Skyllas-Kazacos, J. Membr. Sci. 450 (2014) 313–322.
[43] S. Kim, T.B. Tighe, B. Schwenzer, J. Yan, J. Zhang, J. Liu, Z. Yang, M.A. Hickner, J. Appl. Electrochem. 41 (2011) 1201–1213.
[44] Y. Zeng, X. Zhou, L. An, L. Wei, T. Zhao, J. Power Sources 324 (2016) 738–744.
[45] W. Wang, Z.M. Nie, B.W. Chen, F. Chen, Q.T. Luo, X.L. Wei, G.G. Xia, M. Skyllas-Kazacos, L.Y. Li, Z.G. Yang, Adv. Energy Mater. 2 (2012) 487–493.
[46] Z. Tang, R. Svoboda, J.S. Lawton, D.S. Aaron, A.B. Papandrew, T.A. Zawodzinski, J. Electrochem. Soc. 160 (2013) F1040–F1047.
[47] P. Atkins, J. De Paula, Physical Chemistry for the Life Sciences, Oxford University Press, USA, 2011.
[48] Z. Tang, J.S. Lawton, C.-N. Sun, J. Chen, M.I. Bright, A.M. Jones, A.B. Papandrew, C.H. Fujimoto, T.A. Zawodzinski, J. Electrochem. Soc. 161 (2014) A1860–A1868.
[49] C.-N. Sun, Z. Tang, C. Belcher, T.A. Zawodzinski, C. Fujimoto, Electrochem. Commun. 43 (2014) 63–66.
[50] J.D. Kim, L.J. Ghil, M.S. Jun, J.K. Choi, H.J. Chang, Y.C. Kim, H.W. Rhee, J. Electrochem. Soc. 161 (2014) F724–F728.
[51] S. Kim, T.B. Tighe, B. Schwenzer, J.L. Yan, J.L. Zhang, J. Liu, Z.G. Yang, M.A. Hickner, J. Appl. Electrochem. 41 (2011) 1201–1213.
[52] T. Sukkar, M. Skyllas-Kazacos, J. Appl. Electrochem. 34 (2004) 137–145.
[53] S. Kim, T.B. Tighe, B. Schwenzer, J. Yan, J. Zhang, J. Liu, Z. Yang, M.A. Hickner, J. Appl. Electrochem. 41 (2011) 1201–1213.

Journal of Power Sources 341 (2017) 318–326

Contents lists available at ScienceDirect

Journal of Power Sources

journal homepage: www.elsevier.com/locate/jpowsour

Highly catalytic and stabilized titanium nitride nanowire array-decorated graphite felt electrodes for all vanadium redox flow batteries

L. Wei [a], T.S. Zhao [a, *], L. Zeng [b], Y.K. Zeng [a], H.R. Jiang [a]

[a] Department of Mechanical and Aerospace Engineering, The Hong Kong University of Science and Technology, Clear Water Bay, Kowloon, Hong Kong, China
[b] HKUST Jockey Club Institute for Advanced Study, The Hong Kong University of Science and Technology, Clear Water Bay, Kowloon, Hong Kong SAR, China

HIGHLIGHTS

- Propose a binder-free TiN nanowire array-decorated electrode for VRFBs.
- Energy efficiency is up to 77.4% at 300 mA cm^{-2}, enhancing more than 15%.
- Electrolyte utilization is up to 73.9% at 300 mA cm^{-2}, enhancing more than 43%.
- High stability and capacity retention are achieved by present battery.

GRAPHICAL ABSTRACT

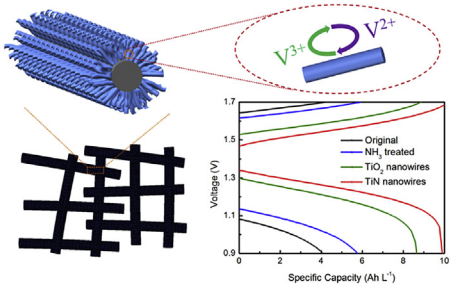

ARTICLE INFO

Article history:
Received 8 August 2016
Received in revised form
14 November 2016
Accepted 5 December 2016
Available online 10 December 2016

Keywords:
Vanadium redox flow battery
Redox chemistry
Electrode
Graphite felt
TiN nanowires

ABSTRACT

In this work, we prepare a highly catalytic and stabilized titanium nitride (TiN) nanowire array-decorated graphite felt electrode for all vanadium redox flow batteries (VRFBs). Free-standing TiN nanowires are synthesized by a two-step process, in which TiO_2 nanowires are first grown onto the surface of graphite felt via a seed-assisted hydrothermal method and then converted to TiN through nitridation reaction. When applied to VRFBs, the prepared electrode enables the electrolyte utilization and energy efficiency to be 73.9% and 77.4% at a high current density of 300 mA cm^{-2}, which are correspondingly 43.3% and 15.4% higher than that of battery assembled with a pristine electrode. More impressively, the present battery exhibits good stability and high capacity retention during the cycle test. The superior performance is ascribed to the significant improvement in the electrochemical kinetics and enlarged active sites toward V^{3+}/V^{2+} redox reaction.

1. Introduction

With increasingly pressing concerns over environmental issues and energy sustainability due to the consumption of fossil fuels, there has been a global agreement that renewable energies such as solar and wind are essential to economic and social development [1–3]. However, the fluctuant and intermittent nature of electricity generated from these renewables makes them less appealing for practical applications [4,5]. Underlying these considerations, the large-scale energy storage technology such as redox flow battery, offering well-established ability to improve grid reliability and utilization with inherent safety, moderate cost, ease of scalability and flexible operation, is an effective method to address this matter [6,7]. Particularly, the vanadium redox flow battery (VRFB) attracts the most attentions, owing to its advantages of significantly low

* Corresponding author.
E-mail address: metzhao@ust.hk (T.S. Zhao).

http://dx.doi.org/10.1016/j.jpowsour.2016.12.016
0378-7753/

cross-contamination and long service life by employing the same element, vanadium, in both positive and negative electrolytes [8,9].

VRFBs store and release electrical energy through electrochemical reactions of the VO_2^+/VO^{2+} and V^{3+}/V^{2+} redox species in the aqueous electrolyte. As a core component of the battery, the electrode provides electroactive surfaces and conducts electrons for redox reactions to take place [10]. Battery polarization, including the activation, ohmic and concentration losses are strongly dependent on the electrode and its surface chemistry [11]. In particular, the activation loss, which is plagued by the poor kinetic reversibility and electrochemical activity towards the vanadium redox reactions, has been a long-term barrier to improve the battery performance during the battery operation [12], often limiting the system to an operating current density lower than 100 mA cm^{-2} [13]. Thus, minimizing the polarization to endow the VRFBs with high energy efficiency at elevated operating current densities, best expressed as high power density, is always desired [14,15]. At the cell level, the augment of power density is effective for decreasing the size of the power stack, including the total area of bipolar plates, electrodes and membranes which represent a significant expense of the battery system [16].

Possessing wide operating potential range, satisfactory chemical and mechanical stability and availability with high electrical conductivity at low cost, carbonaceous materials such as graphite felts have been extensively used as electrodes in the past few decades [17]. Even though carbonaceous electrodes themselves already inherently possess catalytic effects towards vanadium species reactions, the optimization of electrode material is still a necessity to enhance the kinetics of the redox reactions [18]. To date, various surface modification approaches including the acid, thermal and nitrogen treatments have been introduced. While these techniques have been proved to create more active sites for vanadium redox reactions, excessive surface oxidation of carbon material leads to electrode corrosion and eventual disintegration [19]. An alternative approach to increase the active sites is to introduce nanostructured electrocatalysts on the surface of the electrode [20]. To date, a variety of metal-based (metal and metal oxide) and carbon-based materials (carbon nanotube, graphene, and carbon nanoparticles) with high electronic conductivities and specific surface areas have been reported in the literature [21–23]. The performance enhancement varies depending on the distribution uniformity and preparation process of the nanostructured electrocatalysts. High cost of noble metal catalysts as well as tedious synthesis procedures limited their practical application in VRFBs to some extent [24].

In recent years, transition metal carbides, nitrides and carbonitrides have been attracted increasing attention due to their remarkable properties such as high melting point, exceptional chemical stability, and high hardness [25]. Conductivity and catalytic activity of these types of catalysts are also comparable to those of metals [26]. In a recent publication, Wei et al. [27] and Yang et al. [28] performed pioneering work in applying TiC and TiN nanoparticles in aqueous media for catalyzing V^{3+}/V^{2+} redox reaction for VRFBs, respectively. These titanium carbide and nitride nanoparticles were employed to decorate on the surface of carbon fibers via binders to enhance the electrochemical activity of electrodes, enabling a high current-density operation.

In the present work, we propose the use of inexpensive and conductive TiN nanowires as catalysts to enhance the electrochemical activity of the graphite felt. Free-standing TiN nanowires were grown on the surface of graphite felt by a two-step process as illustrated in Fig. 1. TiO_2 nanowires were first grown onto the graphite felt via a seed-assisted hydrothermal method. The samples were subsequently thermally annealed in ammonia gas at a temperature above 700 °C, to convert them to TiN. When applied to flow batteries, the proposed electrode significantly improved the energy efficiency (the ratio of energy between the discharge and charge processes) of a VRFB by enhancing the kinetics of the sluggish V^{3+}/V^{2+} redox reaction, especially under high-power-density operation. In addition, it is demonstrated that the present battery exhibits a significantly improved rate capability and capacity retention during the cycle tests, in comparison to that of a pristine electrode. These superior results suggest that stabilized metal nitride nanomaterials could open up new avenues for the fabrication and application of high-performance electrodes for VRFBs. Fundamental understanding of the catalyst mechanism causing the improvement of battery performance was further discussed.

2. Experimental

2.1. Cyclic voltammetry and electrochemical impedance spectra

Cyclic voltammetry (CV) tests were obtained on a workstation (Autolab, PGSTAT30). A conventional three-electrode electrochemical cell was established with a glassy carbon electrode (GCE) with an area of 0.283 cm^2 as the working electrode, a saturated calomel electrode (SCE) as the reference electrode and a platinum mesh as the counter electrode. The GCE was modified by depositing different catalysts onto it and served as the working electrode as reported elsewhere [27]. 10 mg of commercialized TiN nanoparticles (Aldrich), Vulcan XC-72 carbon nanoparticles (E-TEK) with similar particle size were compared to identify the electrochemical activity of the TiN. These nanoparticles were separately dispersed to 1.9 mL ethanol, to which 0.1 mL of 5 wt% Nafion emulsion was added. After 50 min of sonication, a uniform suspension was achieved and 30 μL of the ink was pipetted on top of the GCE and dried in air. The measurement was performed at −0.7 V to 0 V (vs. SCE) in a solution containing 0.1 M VO^{2+} + 3 M H_2SO_4.

To further determine the rate determining step of the electrode reaction on the graphite felt electrode in this work, an electrochemical impedance spectra (EIS) test was performed with a potentiostat (EG&G Princeton, model 2273). A typical three-electrode system, in which the SGL graphite felt, a platinum mesh, and a saturated calomel electrode (SCE) were employed as the working electrode, counter electrode, and a reference electrode, respectively.

2.2. Fabrication of TiN nanowire decorated electrode

Binder-free TiN nanowires were directly grown on the surface of graphite felt via a two-step process. First, TiO_2 nanowires were grown on the graphite felt using a hydrothermal method as previously reported [29,30]: Graphite felt (SGL company, GFA series, 18 mm × 26 mm) was cleaned with ethanol and dried at 60 °C. Then, the graphite felt was immersed into a 0.2 M $TiCl_4$ aqueous solution (achieved by dissolving 1.10 mL $TiCl_4$ into 48.90 mL concentrated hydrochloric acid) for 30 min and dried in ambient air at room temperature for 10 h, forming the TiO_2 seeds on the surface of the graphite felt. 18.75 mL of concentrated hydrochloric acid, was added into 18.75 mL deionized water, and then mixed with 0.56 mL titanium n-butoxide. This solution, along with the TiO_2 seed coated graphite felt, was transferred to a Teflon-lined stainless autoclave (50 mL volume). The hydrothermal reaction was maintained at a constant temperature of 150 °C for 5.0 h in an electric oven and then cooled at room temperature. The sample was then sonicated with DI water for 5 min and dried at ambient air. This process uniformly covered the entire surface of the carbon fibers by a white film of TiO_2 nanowires. To convert TiO_2 to TiN, the samples were annealed in NH_3 at temperatures of 700, 800, and 900 °C for 1.5 h with a heating rate of 2 °C min^{-1}, respectively. The color of the

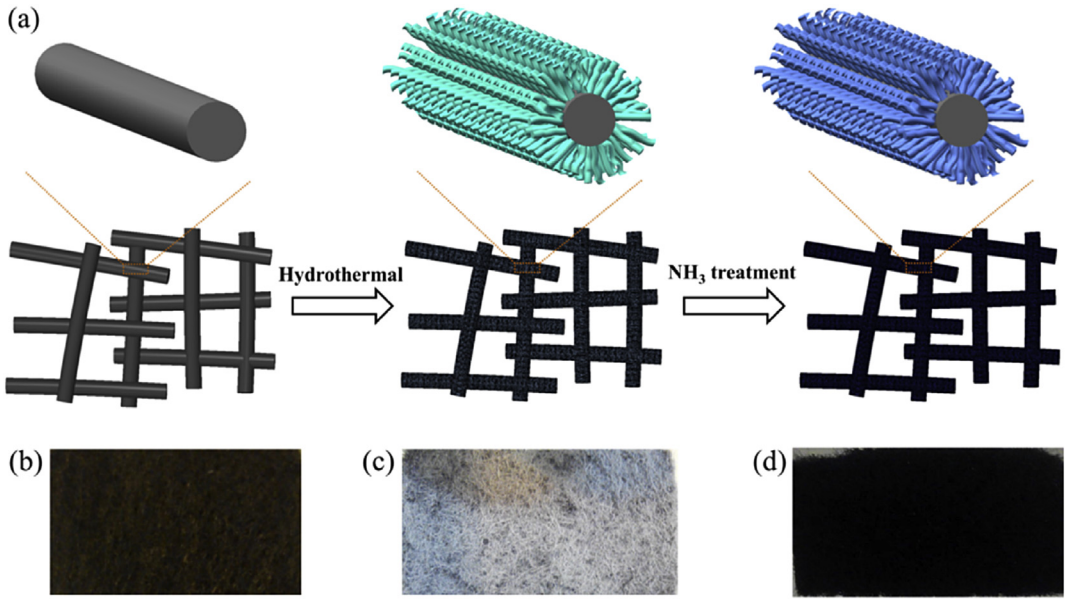

Fig. 1. (a) Schematic diagram of the two-step growth process for preparing TiN nanowires on the surface of graphite felt. Pictures of pristine graphite felt (b), graphite felt coated with TiO_2 nanowires (c), and TiN nanowires prepared in NH_3 atmosphere at 800 °C for 90 min (d).

nanowire film transformed from white to black subsequent to the annealing process, as depicted in Fig. 1d.

2.3. Material characterizations

The morphologies of the graphite felt electrodes were analyzed by scanning electron microscope (JEOL 6700F) at an acceleration voltage of 5.0 kV. Transmission electron-microscopy (TEM) images of TiN nanowires were measured by a high-resolution JEOL 2010F TEM system with a LaB_6 lament at 200 kV. The samples were dispersed in ethanol, sonicated and dripped onto regular carbon-coated Cu grids. The crystal phase and composition of the nanowires were analyzed by a Philips high-resolution X-ray diffraction system (XRD, model PW 1825) using a Cu-Ka source operating at 40 keV and a Micro-Raman spectrophotometer (Renishaw RM 3000) at an excitation wavelength of 514 nm. X-ray photoelectron spectroscopy (XPS) was performed using a Physical Electronics PHI 5600 multi-technique system equipped with an Al monochromatic X-ray source at a power of 350 W.

2.4. Flow battery performance test

Commercially available graphite felt (SGL company, GFA series) with an uncompressed thickness of 1.5 mm (active area of 4.7 cm^2) and prepared TiN nanowire array decorated graphite felt with the same size were used as positive and negative electrode, respectively. The pristine, NH_3 treated, and TiO_2 decorated graphite felts were also used as the negative electrodes for the purpose of comparison. 20 mL solution containing 1 M V^{3+} + 3 M H_2SO_4 and another 20 mL solution containing 1 M VO^{2+} + 3 M H_2SO_4 were employed as the negative and positive electrolytes. Nafion® NR-212 (Dupont) was applied as the membrane. The battery performance was tested in a zero-gap serpentine flow-field structured battery, which is detailed in our previous work [10], as illustrated in Fig. S1. The electrolytes in the batteries were circulated at a fixed flow rate of 0.6 mL s^{-1} with a peristaltic pump (N6-3L, Baoding Shenchen Precision Pump). Before each measurement, nitrogen gas (high purity) was bubbled to exhaust any entrapped air in the electrolyte and reservoirs. All measurements were conducted at room temperature. The performances of the VRFBs were assessed in a battery test system (BT2000, Arbin Instrument, Inc.).

The corresponding theoretical capacity and energy density of the battery in this work are 13.4 Ah L^{-1} and 18.8 Wh L^{-1}, respectively. The detailed calculation method is based on equation $C_{ap} = NC_aF/n$ and $E = NC_aFV/n$ reported by Li et al. [31], where C_{ap} is the capacity, E is the energy density, N is the number of electrons involved in the redox reaction, C_a is the concentration of the active redox species, F is the Faraday constant (26.8 Ah mol^{-1}), V is the voltage of the battery and n is the number of the electrolyte contributing to redox reactions.

3. Results and discussion

A typical transmission electron microscopy (TEM) image of commercialized TiN nanoparticles is shown in Fig. 2a; the average particle size of the TiN nanoparticles ranges from 30 to 50 nm, which is similar to that of the XC-72 carbon nanoparticles (average particle size: 40 nm) [10]. To identify the catalytic effect of TiN, CV measurements of commercialized TiN nanoparticles and XC-72 carbon nanoparticles toward V^{3+}/V^{2+} redox couple were compared and the results are shown in Fig. 2b. For the carbon nanoparticles electrode, poorly formed redox oxidation and reduction peaks are observed, indicating the catalytic activity of the electrode towards the V^{3+}/V^{2+} redox couple is rather low. It is also worth noting that the cathode current increases sharply as a result of the hydrogen evolution reaction at a more negative potential than −0.55 V (vs. SCE). The hydrogen evolution reaction appears to have a significant influence on the V^{3+} to V^{2+} reduction reaction on the carbon nanoparticles electrode [32]. As for the TiN electrode, a more pronounced redox peak appears as depicted from the CV curve. The anodic and cathodic peak currents for the redox reactions are considerably increased, and the peak potential separation is approximately 122 mV with a scan rate of 50 mV s^{-1}. This implies that the poor performance of the V^{3+}/V^{2+} couple is significantly enhanced by improving the electron transfer kinetics [33–35]. Furthermore, the onset potential of hydrogen evolution on the TiN electrode is significantly decreased compared with that on carbon nanoparticles, which implies that undesired side reaction in

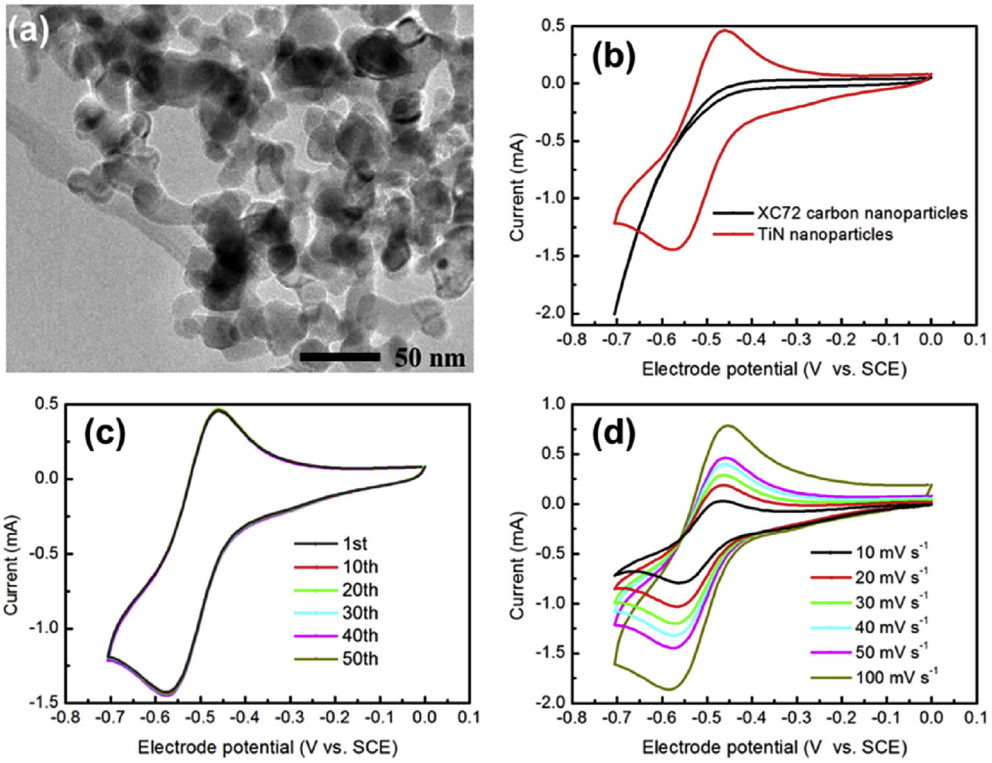

Fig. 2. (a) Typical TEM image of commercial TiN nanoparticles; (b) cyclic voltammograms for different electrode materials at a scan rate of 50 mV s^{-1} in a solution containing 0.1 M VO^{2+} and 3 M H_2SO_4; (c) repeating sweeping measurement of TiN nanoparticles at a scan rate of 50 mV s^{-1}; (d) cyclic voltammograms recorded on TiN nanoparticles at various scan rates.

VRFB systems, hydrogen evolution reaction, is also substantially suppressed [36]. Repetitive CVs were performed (50 scans at 50 mV s^{-1}, see Fig. 2c) to identify the durability of TiN as a catalyst for the redox reactions of the vanadium species. It is found that the curves exhibit good repeatability without significant degradation and the value of the anode peak current/cathode peak current remains essentially the same throughout the entire test process, which can be perceived as a first indication of the electrode stability. Fig. 2d displays the CV curves of TiN at different scan rates. The linear relationship ($R^2 = 0.993$ and $R^2 = 0.991$) between the anodic and cathodic peak currents and the square root of the scan rate observed on the TiN electrode indicates that the redox reaction is limited by its transport in the electrolyte in the range of scan rates [37].

The morphological structures of the TiN nanowires were performed by SEM characterization. Fig. 3a–c shows the representative morphology of the original graphite felt. From these figures it is seen that the carbon fibers are well-interconnected. The surface of the graphite felt is smooth without observable defects, providing an appropriate substrate for the growth of TiO_2 nanowires. The porous architecture of the electrode can facilitate the mass transport of the electrolyte during the charge/discharge processes [5,38]. After the hydrothermal reaction, a dense TiO_2 nanowire coverage was obtained due to well-dispersion of the precursor seeds (see Fig. 3d–f). These stabilized nanowires are directly linked to the surface of the graphite felt without any binder. A binder-free structure avoids the use of expensive Nafion suspensions, which not only helps to decrease the capital cost of the system [39], but also exposes the active surface of the electrode to the electrolytes to a larger extent since binders could potentially cover effective surface active sites for the redox reactions [40]. Further conversion of TiO_2 to TiN by annealing the samples in NH_3 at temperatures of 700, 800, and 900 °C was obtained and the results are shown in Fig. 3g–i, respectively. The morphology of the original TiO_2 nanowires is observed to be well-preserved at a temperature below 800 °C. However, when further heating at 900 °C, the original nanostructure was severely damaged. A majority of the nanowires collapsed and detached from the surface of graphite felt fibers. Therefore, increasing the heat treatment temperature benefits the nitridation reaction that converts TiO_2 to TiN [41], but leads to the destruction of the electrocatalysts nanostructures, which decreases the surface area and stability of the electrode. In this regard, an upper limit of the nitridation temperature at 800 °C is established in the following investigation.

To evaluate the physical properties of the obtained nanowires, XRD measurements were conducted to confirm the conversion of TiO_2 to TiN at different temperatures and the results are shown in Fig. 4a. The original TiO_2 sample shows several intense peaks of rutile TiO_2 (JCPDS: 21-1276). After the nitridation reaction occurred at a temperature above 700 °C, the obtained samples exhibit diffraction peaks at 36.7°, 42.6°, 61.8°, corresponding to the (111), (200) and (220) planes of the cubic TiN phase (JCPDS: 65-0714) [41]. Raman analyses are shown in Fig. 4b, it is found that the TiO_2 sample displays four characteristic peaks at around 145, 236, 445 and 609 cm^{-1}, which is attributed to the rutile TiO_2. After the nitridation reaction, it is observed that the Raman spectra is greatly changed and the TiN phase corresponding to the peaks at around 201, 323 and 552 cm^{-1} appear [29], indicating that the rutile TiO_2 could be completely converted to cubic TiN after annealing in NH_3 at a temperature of 800 °C, consistently with the results from XRD.

To further investigate the surface property of the samples, a contact angle measurement was performed by using the typical droplet method. As shown in Fig. S2, the wettability becomes significantly different in samples depending on the surface

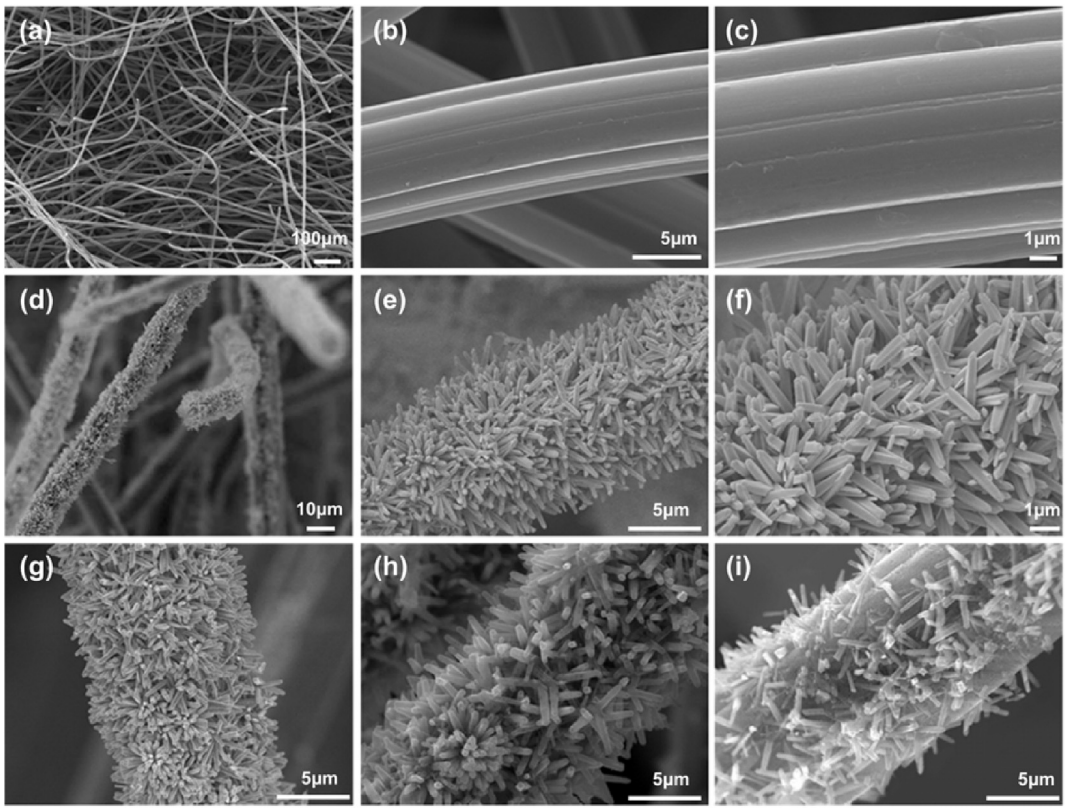

Fig. 3. SEM images collected for the original graphite felt (a–c); TiO_2 decorated electrode (d–f); and TiO_2 nanowires annealed in NH_3 at temperature of (g) 700 °C, (h) 800 °C, and (i) 900 °C.

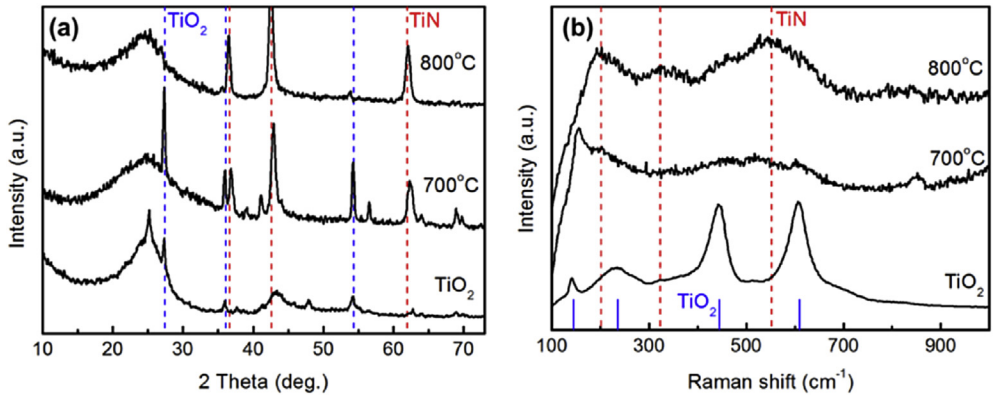

Fig. 4. XRD spectra (a) and Raman spectra (b) collected from TiO_2 and TiO_2 nanowires annealed in NH_3 at 700 and 800 °C. The blue and red dashed lines highlight peaks corresponding to rutile TiO_2 and cubic phase TiN, respectively. (For interpretation of the references to colour in this figure legend, the reader is referred to the web version of this article.)

modification process. Depending on the results, the measured contact angle is 120° for the pristine graphite felt. In contrast, it was difficult to measure the contact angle of TiO_2 and TiN (annealed at 800 °C) samples because it is immediately soaked when introduced to water, which indicates that the nature of electrode surface changes from hydrophobic to super hydrophilic through decoration of these nanowires. Eventually, improved electrolyte accessibility would be favorable for VRFB performance [42].

The crystal structure of the obtained TiN nanowires was analyzed further by high-resolution transmission electron microscopy (HRTEM). The sample was prepared by dropping nanowires onto the regular carbon film grid. As shown in Fig. S3, the diameters of the nanowires are in the range of 150–250 nm. Fig. 5a shows the HRTEM image of single typical nanowire. It can be seen from the figure that the exposed edges of TiN nanowire might act as active sites toward the redox reactions [36]. Fig. 5b displays the image of the crystal structure of the nanocrystals. The image reveals that the deposited nanowire possesses a high degree of crystallinity with an interfringe distance of about 0.2482 nm, which can be indexed to the (111) plane of the face-centered cubic-structured TiN. The high crystallinity can be also demonstrated from the fast Fourier transform (FFT) pattern, as presented inset of Fig. 5b.

To have an in-depth understanding of the surface chemical structures and oxidation state of the nanowires, energy dispersive

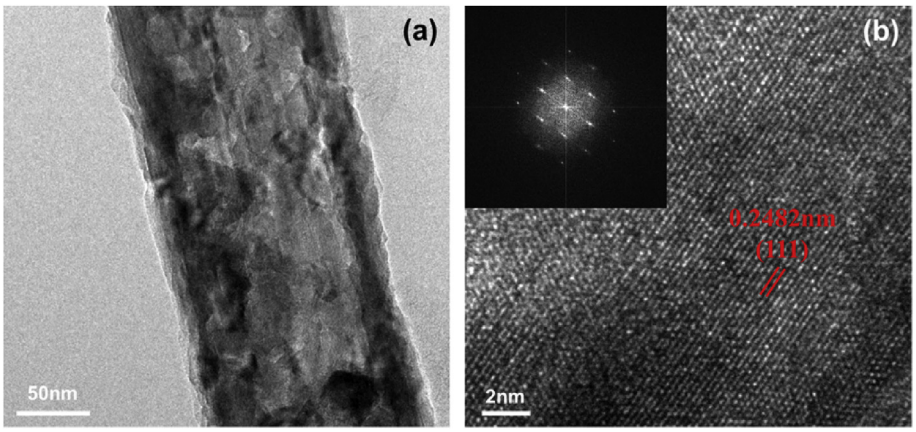

Fig. 5. (a) HRTEM image of one typical nanowire, (b) crystal structure of the TiN (nitrided at 800 °C) nanocrystals and corresponding fast Fourier transform (FFT) pattern.

X-ray spectroscopy (EDS) and XPS characterizations were determined and the results are shown in Fig. S4 and Fig. 6. EDS elemental mapping results show that the elements are uniformly distributed in the nanowire. A trace amount of oxygen detected suggests the presence of TiO_2 or TiO_xN_y in the TiN nanowires. XPS spectra of the TiN nanowires confirm the presence of N, while no N signal is found for the pristine TiO_2 samples, as expected. The Ti 2p spectrum of the pristine TiO_2 exhibits the binding energy of 459.3 eV ascribed to the Ti 2p3/2 of TiO_2 nanowires [30]. It is noteworthy to mention that, after nitridation, multiple peaks are deconvoluted at lower binding energies, which can be assigned to be Ti–N ($2p_{3/2}$ = 455.6–455.9 eV and $2p_{1/2}$ = 461.4–461.8 eV), Ti–N–O ($2p_{3/2}$ = 457.1–457.5 eV and $2p_{1/2}$ = 463.1–463.5 eV), and Ti–O ($2p_{3/2}$ = 458.7–459.3 eV and $2p_{1/2}$ = 464.4–465.0 eV) [43]. The residual Ti–O bond on the surface is mainly attributed to the inefficient nitridation and partial oxidation in the ambient air [44]. The fact that new Ti–N–O and Ti–N peaks appeared during nitradation indicates that the surface of NH_3-treated TiO_2 nanowire is composed of Ti–N–O, Ti–N, and Ti–O chemical states [29].

To demonstrate the practical application of the proposed electrode in the VRFB, the electrochemical properties of the TiN nanowires decorated graphite felt were further studied by typical charge–discharge measurements. Fig. 7a shows the voltage profiles of batteries at the same current density of 300 mA cm^{-2}. The original graphite felt, NH_3-treated and TiO_2 nanowires decorated electrode are employed as references, respectively. Under the fixed voltage region between 0.9 and 1.7 V, the cell employing pristine graphite felt exhibits poor discharge capacity (4.1 Ah L^{-1}, 30.6% of theoretical capacity), indicating that battery performance is low due to severe polarization. This is mainly caused by an insufficient number of surface active sites for the vanadium redox reactions on the electrode. In comparison to the pristine electrode, the NH_3 treated one displays a slightly reduced overpotential and increased capacity (5.7 Ah L^{-1}, 42.5% of theoretical capacity) in both charge and discharge processes owing to the presence of nitrogen functional groups. However, it is worth mentioning that an excess of these kind of surface functional groups could reduce the electron conductivity of the electrode, thus leading to increased ohmic loss during high current density operation [19]. For the electrode decorated with TiO_2 nanowires (8.6 Ah L^{-1}, 64.2% of theoretical capacity), the overpotentials further decreased in the corresponding charge and discharge processes due to improved hydrophilicity and an enlarged electrochemical surface area. More impressively, the cell installed with the TiN nanowires electrode exhibits the largest capacity (9.9 Ah L^{-1}, 73.9% of theoretical capacity), lowest charge voltage plateau, and highest discharge voltage plateau. This indicates that the TiN decorated electrode shows superior electrochemical properties compared with the original, N-doped and TiO_2 decorated electrodes. The superior electrochemical performance can be attributed to the surface properties of the TiN nanowires. Specifically, the conductive and hydrophilic layer of the TiN, as well as its high surface area with abundant active sites, greatly accelerates the redox reaction, especially at high charge/discharge rates, presumably by lowering the kinetic activation energy for the redox reaction [12]. The improvement in the specific capacity, which is identified as increased utilization of the electrolyte [45,46], will contribute efficiently to capital cost reduction as vanadium salts account for nearly 40% of the system cost [47].

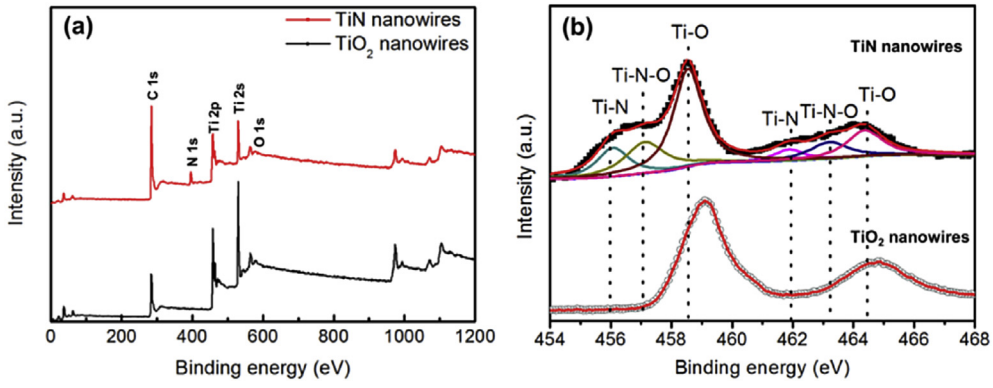

Fig. 6. XPS survey (a) and Ti 2p XPS spectra (b) of the TiO_2 and TiN nanowire (nitrided at 800 °C) decorated electrode.

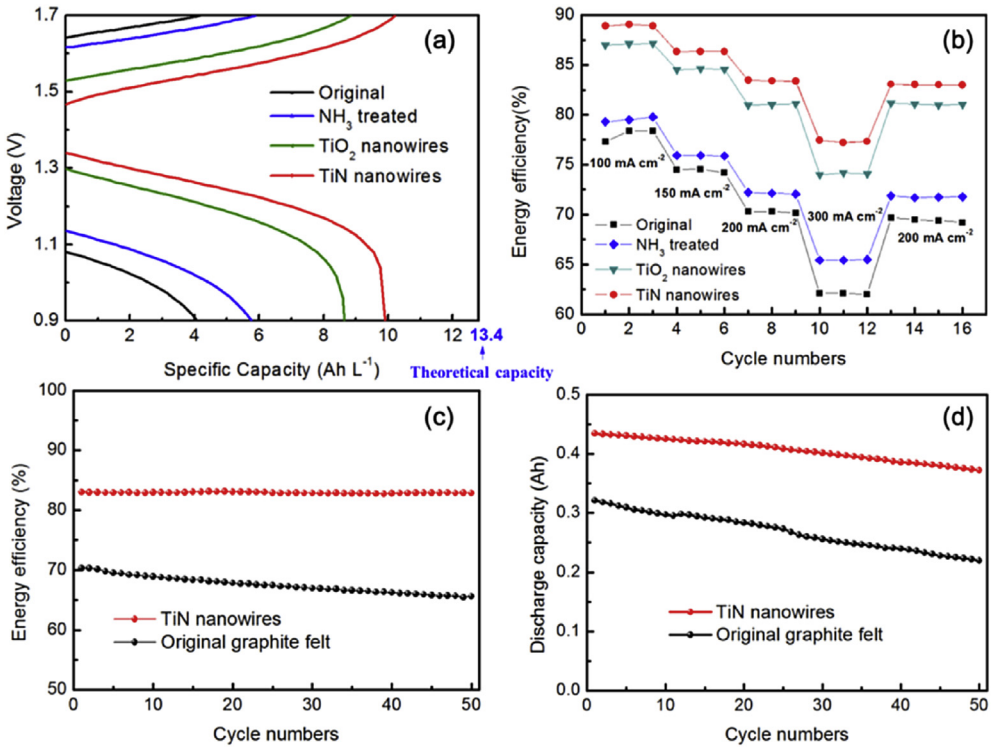

Fig. 7. Electrochemical performance of VRFBs quipped with pristine, NH_3 treated, TiO_2 decorated and TiN nanowire (nitrided at 800 °C) array-decorated graphite felt electrodes. (a) Charge and discharge curve at 300 mA cm^{-2}; (b) energy efficiency as a function of cycle number at different current densities. Cycling tests of VRFBs with and without TiN nanowire decorated electrode: (c) energy efficiency and (d) discharge capacity of VRFBs at a current density of 200 mA cm^{-2}.

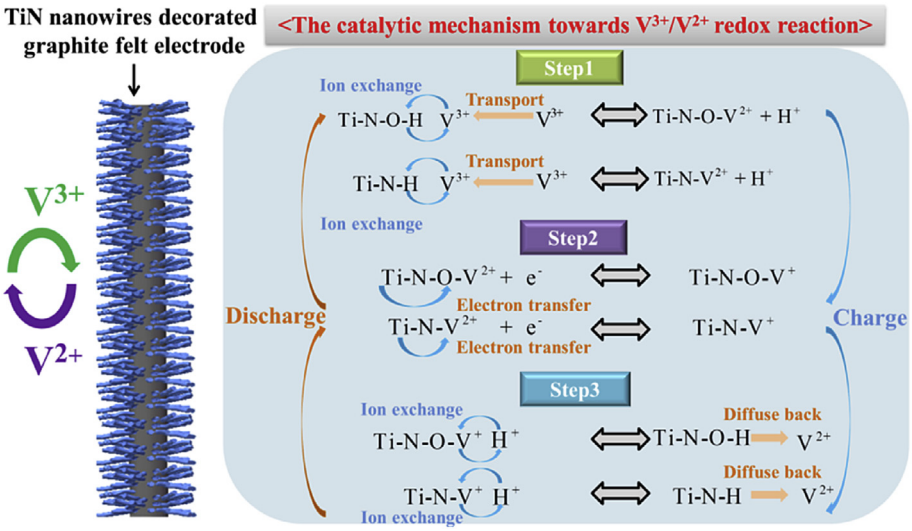

Fig. 8. Schematic illustration of the mechanism for the V^{3+}/V^{2+} redox reaction occurring in the presence of TiN nanowires on the surface of graphite felt electrode.

Additionally, the rate capability test of the samples was performed as increasing current densities from 100 to 300 mA cm^{-2} (see Fig. 7b). After being decorated with TiN nanowire arrays, the battery exhibits a substantially improved rate capability, as expected. Even at a current density as high as 300 mA cm^{-2}, the energy efficiency reaches 77.4%, which is 15.4%, 12% and 3.5% higher than that of the battery with pristine, NH_3 treated and TiO_2 nanowires decorated graphite felt electrode, respectively. Notably, to assess the stability of the TiN decorated electrode, the operating current from 300 to 200 mA cm^{-2} at the thirteenth cycle is swiftly changed and noted that the battery performance was fully recovered, indicating that the chemical and electrochemical robustness of the TiN decorated electrode in negative electrolyte [11].

A VRFB's stability is of critical importance for practical applications [47]. To further identify the stability and suitability of the proposed electrode during battery operation, cycling tests of VRFBs with and without TiN decorated electrodes were conducted at a current density of 200 mA cm^{-2}. As depicted in Fig. 7c, the energy efficiency of the battery with the proposed electrode sustained an enhanced initial improvement of 13% compared to that of the

pristine battery and the value stayed at above 82.8% without observable decay. Fig. 7d displays corresponding discharge capacities within cycles. The capacity of the present battery maintained above 86% of the initial value after 50 cycles, displaying an average capacity decay rate of merely 0.28% per cycle, equaling to apparently higher capacity retention compared to that of the pristine electrode. These results further demonstrate the excellent stability of the electrocatalytic effect brought by TiN nanowires over repeated cycling. On the basis of the experimental results, the TiN nanowires decorated electrode was proved to be an effective electrode in the VRFB system primarily due to their high catalytic activity towards the V^{3+}/V^{2+} redox reaction. According to our EIS test results (see Fig. S5), the charge transfer resistance of V^{3+}/V^{2+} and VO_2^+/VO^{2+} redox on the graphite felt is 14.96 and 0.91 Ω cm^2, respectively. The VO_2^+/VO^{2+} redox couple shows much more facile kinetics than the V^{3+}/V^{2+} couple, which indicates that catalysis efforts should be focused on V^{3+}/V^{2+} in the negative side rather than the VO_2^+/VO^{2+} in the positive side (in consistence with the kinetic studies of vanadium redox couples reported by Prof. Mench [48,49] and Shao-Horn group [50]).

Through clear confirmation of the performance improvement by introducing TiN nanowires, a possible explanation for the catalytic mechanism for the vanadium redox reaction can be speculated guided by the early study of Skyllas-Kazacos et al. [51,52], as shown in Fig. 8. Taking the charge process as an example; the first step in the reaction involves an ion exchange process between V^{3+} ions transported from the bulk of the electrolyte and the hydrogen ions of the Ti—N—O—H and Ti—N—H. Thus, V^{3+} ions can be absorbed with ease on the Ti—N and Ti—N—O functional layer. In the second step, electron transfer, facilitated by Ti—N and Ti—N—O bonds acting as an electron donor, takes place from V^{3+} to V^{2+} along the bonds. In the final step, the reduction reaction is terminated by an ion-exchange between the V^{2+} formed on the electrode surface and the hydrogen ions in the electrolyte. During the discharge process, a similar oxidation reaction in the opposite direction occurs. It is worth mentioning that the pristine TiO_2 has a large band-gap and low electrical conductivity, but the band-gap deceases and electrical conductivity enhances after the N-doping process [53,54]. Yang et al. [55] investigated the effect of N concentrations on the electrical conductivity of TiO_2. They found that as the N concentration increased from 0 to 1.39%, and then to 4.17%, TiO_2 gradually transformed to metallic states. The increasing electrical conductivity from TiO_2 to TiN provides an explanation for the better battery performance of TiN than TiO_2 decorated electrode.

4. Conclusion

In summary, using a two-step approach, we synthesized a highly catalytic and binder-free TiN nanowire array decorated graphite felt electrode for VRFBs. Substantial enhancement in battery performance, including energy efficiency and utilization of the electrolyte, is attributed to the outstanding catalytic effect of decorated TiN nanowires on the surface of the electrode. Even at a current density of as high as 300 mA cm^{-2}, the energy efficiency reached 77.4%, and the utilization of electrolyte reached 73.9% of the theoretical capacity, which is among the highest performance of VRFBs recorded in the literature. Moreover, the battery equipped with the proposed electrode was demonstrated to show excellent stability and high capacity retention during the cycling test. It is believed that this work offers a new approach for fabricating high-performance electrode, and contributes to the development of transition metal nitrides nanomaterials in VRFB technology to achieve a superior battery performance.

Acknowledgements

The work described in this paper was fully supported by a grant from the Research Grants Council of the Hong Kong Special Administrative Region, China (Project No. 623313).

Appendix A. Supplementary data

Supplementary data related to this article can be found at http://dx.doi.org/10.1016/j.jpowsour.2016.12.016.

References

[1] Q. Xu, T.S. Zhao, Prog. Energy Combust. Sci. 49 (2015) 40–58.
[2] P.K. Leung, X. Li, C. Ponce de León, L. Berlouis, C.T.J. Low, F.C. Walsh, RSC Adv. 2 (2012) 10125.
[3] C. Ding, H.M. Zhang, X.F. Li, T. Liu, F. Xing, J. Phys. Chem. Lett. 4 (2013) 1281–1294.
[4] R.M. Darling, K.G. Gallagher, J.A. Kowalski, S. Ha, F.R. Brushett, Energy & Environ. Sci. 7 (2014) 3459–3477.
[5] P. Leung, M. Mohamed, A. Shah, Q. Xu, M. Conde-Duran, J. Power Sources 274 (2015) 651–658.
[6] J. Noack, N. Roznyatovskaya, T. Herr, P. Fischer, Angew. Chem. Int. Ed. 54 (2015) 9776–9809.
[7] K. Lin, Q. Chen, M.R. Gerhardt, L. Tong, S.B. Kim, L. Eisenach, A.W. Valle, D. Hardee, R.G. Gordon, M.J. Aziz, Science 349 (2015) 1529–1532.
[8] M. Skyllas-Kazacos, M.H. Chakrabarti, S.A. Hajimolana, F.S. Mjalli, M. Saleem, J. Electrochem. Soc. 158 (2011) R55.
[9] X.L. Zhou, T.S. Zhao, L. An, L. Wei, C. Zhang, Electrochim. Acta 153 (2015) 492–498.
[10] L. Wei, T. Zhao, G. Zhao, L. An, L. Zeng, Appl. Energy 176 (2016) 74–79.
[11] P.K. Leung, J. Palma, E. Garcia-Quismondo, L. Sanz, M. Mohamed, M. Anderson, J. Power Sources 310 (2016) 1–11.
[12] K.J. Kim, H.S. Lee, J. Kim, M.S. Park, J.H. Kim, Y.J. Kim, M. Skyllas-Kazacos, ChemSusChem 9 (2016) 1329–1338.
[13] B. Sun, M. Skyllas-Kazacos, Electrochim. Acta 37 (1992) 2459–2465.
[14] X.L. Zhou, Y.K. Zeng, X. Zhu, L. Wei, T.S. Zhao, J. Power Sources 325 (2016) 329–336.
[15] Y. Zeng, X.L. Zhou, L. An, L. Wei, T.S. Zhao, J. Power Sources 324 (2016) 738–744.
[16] D.S. Aaron, Q. Liu, Z. Tang, G.M. Grim, A.B. Papandrew, A. Turhan, T.A. Zawodzinski, M.M. Mench, J. Power Sources 206 (2012) 450–453.
[17] K.J. Kim, Y.-J. Kim, J.-H. Kim, M.-S. Park, Mater. Chem. Phys. 131 (2011) 547–553.
[18] A. Parasuraman, T.M. Lim, C. Menictas, M. Skyllas-Kazacos, Electrochim. Acta 101 (2013) 27–40.
[19] A. Di Blasi, O. Di Blasi, N. Briguglio, A.S. Aricò, D. Sebastián, M.J. Lázaro, G. Monforte, V. Antonucci, J. Power Sources 227 (2013) 15–23.
[20] M. Park, J. Ryu, J. Cho, Chem. Asian J. 10 (2015) 110.
[21] Z. Gonzalez, S. Vizireanu, G. Dinescu, C. Blanco, R. Santamaria, Nano Energy 1 (2012) 833–839.
[22] M. Ulaganathan, A. Jain, V. Aravindan, S. Jayaraman, W.C. Ling, T.M. Lim, M.P. Srinivasan, Q. Yan, S. Madhavi, J. Power Sources 274 (2015) 846–850.
[23] P. Han, Y. Yue, Z. Liu, W. Xu, L. Zhang, H. Xu, S. Dong, G. Cui, Energy & Environ. Sci. 4 (2011) 4710.
[24] B. Li, M. Gu, Z. Nie, Y. Shao, Q. Luo, X. Wei, X. Li, J. Xiao, C. Wang, V. Sprenkle, W. Wang, Nano Lett. 13 (2013) 1330–1335.
[25] S.T. Oyama, Catal. Today 15 (1992) 179–200.
[26] H.H. Hwu, J.G.G. Chen, Chem. Rev. 105 (2005) 185–212.
[27] L. Wei, T.S. Zhao, L. Zeng, X.L. Zhou, Y.K. Zeng, Energy Technol. Ger. 4 (2016) 990.
[28] C.M. Yang, H.N. Wang, S.F. Lu, C.X. Wu, Y.Y. Liu, Q.L. Tan, D.W. Liang, Y. Xiang, Electrochim. Acta 182 (2015) 834–840.
[29] X.H. Lu, G.M. Wang, T. Zhai, M.H. Yu, S.L. Xie, Y.C. Ling, C.L. Liang, Y.X. Tong, Y. Li, Nano Lett. 12 (2012) 5376–5381.
[30] G.M. Wang, H.Y. Wang, Y.C. Ling, Y.C. Tang, X.Y. Yang, R.C. Fitzmorris, C.C. Wang, J.Z. Zhang, Y. Li, Nano Lett. 11 (2011) 3026–3033.
[31] B. Li, Z.M. Nie, M. Vijayakumar, G.S. Li, J. Liu, V. Sprenkle, W. Wang, Nat. Commun. 6 (2015).
[32] P.K. Leung, C. Ponce-de-León, C.T.J. Low, A.A. Shah, F.C. Walsh, J. Power Sources 196 (2011) 5174–5185.
[33] L. Shi, S.Q. Liu, Z. He, J.X. Shen, Electrochim. Acta 138 (2014) 93–100.
[34] M. Park, J. Ryu, Y. Kim, J. Cho, Energy & Environ. Sci. 7 (2014) 3727–3735.
[35] M. Park, I.Y. Jeon, J. Ryu, J.B. Baek, J. Cho, Adv. Energy Mater 5 (2015).
[36] M. Park, Y.J. Jung, J. Kim, H. Lee, J. Cho, Nano Lett. 13 (2013) 4833–4839.
[37] J.H. Kim, K.J. Kim, M.S. Park, N.J. Lee, U. Hwang, H. Kim, Y.J. Kim, Electrochem. Commun. 13 (2011) 997–1000.
[38] S.Y. Wang, X.S. Zhao, T. Cochell, A. Manthiram, J. Phys. Chem. Lett. 3 (2012) 2164–2167.
[39] M.L. Perry, A.Z. Weber, J. Electrochem. Soc. 163 (2016) A5064–A5067.
[40] G. Sasikumar, J.W. Ihm, H. Ryu, Electrochim. Acta 50 (2004) 601–605.

[41] Y. Ren, Z. Ren, J. Li, S. Wang, J. Yu, RSC Adv. 5 (2015) 106439–106443.
[42] H. Zhou, J. Xi, Z. Li, Z. Zhang, L. Yu, L. Liu, X. Qiu, L. Chen, RSC Adv. 4 (2014) 61912–61918.
[43] I. Milosev, H.H. Strehblow, B. Navinsek, M. Metikoshukovic, Surf. Interface Anal. 23 (1995) 529–539.
[44] Y.J. Wei, C.W. Peng, T.M. Cheng, H.K. Lin, Y.L. Chen, C.Y. Lee, H.T. Chiu, Acs Appl. Mater Inter 3 (2011) 3804–3812.
[45] Q. Zheng, F. Xing, X.F. Li, T. Liu, Q.Z. Lai, G.L. Ning, H.M. Zhang, J. Power Sources 266 (2014) 145–149.
[46] A. Di Blasi, N. Briguglio, O. Di Blasi, V. Antonucci, Appl. Energy 125 (2014) 114–122.
[47] Y. Zeng, T. Zhao, L. An, X. Zhou, L. Wei, J. Power Sources 300 (2015) 438–443.
[48] D. Aaron, C.N. Sun, M. Bright, A.B. Papandrew, M.M. Mench, T.A. Zawodzinski, Ecs Electrochem Lett. 2 (2013) A29–A31.
[49] C.N. Sun, F.M. Delnick, D.S. Aaron, A.B. Papandrew, M.M. Mench, T.A. Zawodzinski, Ecs Electrochem Lett. 2 (2013) A43–A45.
[50] N. Pour, D.G. Kwabi, T. Carney, R.M. Darling, M.L. Perry, Y. Shao-Horn, J. Phys. Chem. C 119 (2015) 5311–5318.
[51] K.J. Kim, M.S. Park, Y.J. Kim, J.H. Kim, S.X. Dou, M. Skyllas-Kazacos, J. Mater Chem. A 3 (2015) 16913–16933.
[52] S. Zhong, M. Skyllas-Kazacos, J. Power Sources 39 (1992) 1–9.
[53] A. Nambu, J. Graciani, J. Rodriguez, Q. Wu, E. Fujita, J.F. Sanz, J. Chem. Phys. 125 (2006) 094706.
[54] C. Di Valentin, E. Finazzi, G. Pacchioni, A. Selloni, S. Livraghi, M.C. Paganini, E. Giamello, Chem. Phys. 339 (2007) 44–56.
[55] K. Yang, Y. Dai, B. Huang, J. Phys. Chem. C 111 (2007) 12086–12090.

Journal of Power Sources 342 (2017) 9–16

Contents lists available at ScienceDirect

Journal of Power Sources

journal homepage: www.elsevier.com/locate/jpowsour

An aprotic lithium/polyiodide semi-liquid battery with an ionic shield

Y.X. Ren [a, 1], M. Liu [a, 1], T.S. Zhao [a, *], L. Zeng [b], M.C. Wu [a]

[a] Department of Mechanical and Aerospace Engineering, The Hong Kong University of Science and Technology, Clear Water Bay, Kowloon, Hong Kong Special Administrative Region
[b] HKUST Jockey Club Institute for Advanced Study, The Hong Kong University of Science and Technology, Clear Water Bay, Kowloon, Hong Kong SAR, China

HIGHLIGHTS

- An ion selective aprotic Li/polyiodide semi-liquid battery was demonstrated.
- The polyiodide shuttles can be suppressed by the electrostatic repulsion.
- A high energy density of 170.5 Wh L^{-1} was attained with 1.5 M LiI_3 catholyte.
- Stable cycling was achieved with a capacity retention over 84% for 100 cycles.

GRAPHICAL ABSTRACT

Graphical abstract

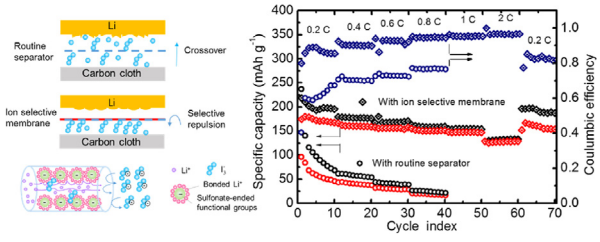

ARTICLE INFO

Article history:
Received 7 October 2016
Received in revised form
9 December 2016
Accepted 12 December 2016
Available online 16 December 2016

Keywords:
Lithium/polyiodide battery
Shuttle effect
Ion selective membrane
Electrostatic repulsion

ABSTRACT

In this paper, we report a high-energy-density lithium/polyiodide (Li/PI) semi-liquid battery with soluble polyiodide in ether-based solvents as the catholyte. The challenge of shuttle effect is addressed by adopting a hybrid membrane coated with negatively charged sulfonate-ended perfluoroalkyl polymer, which allows for inhibition of polyiodide shuttles due to the electrostatic repulsion. The assembled Li/PI battery demonstrates a superior volumetric energy density (170.5 Wh L^{-1}), a stable cycling performance (>100 cycles, averaged decay < 0.16% at 0.2 C), a high energy efficiency (>84%, 100 cycles at 2 C), and a high coulombic efficiency (>95%, 100 cycles at 2 C). These high performances achieved suggest that the aprotic Li/polyiodide battery with a compact architecture has the potential for various energy storage applications.

1. Introduction

The development of high-energy-density and efficient scaled-up electrical energy storage (EES) systems becomes a focal point for distributed electric grids, especially with the ever-increasing deployment of wind and solar powers, which suffers from their intermittent and fluctuating nature [1–5]. Among the existing EES systems, lithium based batteries promise superior energy density and excellent reversibility, thus the efforts to innovate the lithium based batteries for scaled-up energy storage have never ceased [6–12]. Beyond using solid-state cathode host for Li-ions, exploring strategies to dissolve the active material in the solution phase catholyte have drawn increasing attentions, which are attributed to their underlying superiorities of (i) faster mass transport in the liquid phase catholyte, (ii) more facile electron transfer across a liquid/solid interface and (iii) the flexibility of designing the scaled-up systems with decoupled energy storage and power output [13–16].

In light of these merits, Lu and Goodenough proposed the prototype of a hybrid semi-liquid battery using an alkaline metal (for example, lithium metal) and an aqueous cathode containing redox-

* Corresponding author.
E-mail address: metzhao@ust.hk (T.S. Zhao).
[1] These authors contributed equally to this work.

http://dx.doi.org/10.1016/j.jpowsour.2016.12.043
0378-7753/

active species (for example, ferricyanide), separated by a glass ceramic membrane [17,18]. Also employing the aqueous cathode configuration, Zhao et al. conceived a series of development for halogen-based cathodes, demonstrating remarkable battery performances, especially in terms of the energy density and cycling stability [19–23]. However, the critical demand for a crack-free glass ceramic membrane renders it challenging to scale up the lithium/aqueous configuration. Due to the fragile and resistive nature of the solid state electrolyte, it is still on its pathway to meet the requirement of developing a sufficiently robust Li/aqueous system.

The application of non-aqueous catholytes possibly mitigates the above inconvenience. Towards high-energy-density storage and stable performance, redox-active species in non-aqueous systems are under exploration. One direction is the organic redox compounds (e.g., ferrocene-based, TEMPO-based), which is still an ongoing effort [14,15]. The other concerns for the efficient utilization of the inorganic redox couples including iron, halogen and chalcogen-based redox couples [20]. For such batteries, the solubility and the stability of the redox couples to pair with the lithium anode become target issues to be considered. Recently, emerging efforts have been paid in developing non-aqueous Li-S flow batteries. The Li-S battery chemistry enables a relatively stable passivation layer on the Li anode, which possibly realizes a membrane-free design, however, due to the inferior solubility of short-chain Li_2S_n (n = 1, 2, 4), the recently developed Li-S flow battery with a volumetric energy density of 30 Wh L^{-1} didn't exhibit superior advantages over the vanadium redox flow battery (VRFB) systems (25 Wh L^{-1}) [13,24]. Towards a higher energy density, one of the promising alternatives is the I_3^-/I^- redox couple, which is capable of simultaneously compromising among the demands of fast reaction kinetics, non-toxicity nature and high solubility [22,23,25]. During the discharge-charge process, the cathodic reaction occurs as $I_3^- + 2e^- \leftrightarrow 3I^-$. By using a 3 M LiI catholyte for example, the volumetric capacity can reach as high as 53.5 A h L^{-1}, resulting in a volumetric energy density around 150 Wh L^{-1}, which far more exceeds the conventional redox flow batteries [26].

With the high solubility of polyiodide in the aprotic solvents (~9 M I^- in DOL/DME), self-discharge as well as infinite charging is a serious problem facing such aprotic Li/PI batteries. On the Li anode surface, polyiodide anions can be chemically or electrochemically reduced to iodide anions ($2Li + I_3^- \rightarrow 2Li^+ + 3I^-$ or $I_3^- + 2e^- \rightarrow 3I^-$), lowering the battery's coulombic efficiency. For those reported Li/iodine batteries, approaches for immobilizing the iodine into a host material (e.g. carbon) were exploited [27,28]. However, binding between the carbon materials and polyiodide species was found to be intrinsically weak [28]. Unlike polysulfides, it is challenging to identify suitable materials to chemically anchor the polyiodide [29]. On the other hand, lithium nitrate as an electrolyte additive has been introduced into the Li/iodine batteries, which contributes to generate a chemically stable passivation layer onto the Li anode to retard the shuttle effect [28,30]. Unfortunately, the multidimensional Li growth during the cycling process usually leads to the collapse of the passivation layer [31–33]. Due to above reasons, to our knowledge, the aprotic semi-liquid Li/polyiodide battery that directly utilizes the liquid catholyte, has not been reported until today. In addition to above strategies, we note that for cation exchange membranes (CEMs) in fuel cells and chlor-alkali industry, anions can be excluded from CEMs by an electrostatic repulsion from the negatively charged functional groups on the membrane, which is a phenomenon referred to as the Donnan exclusion [34–37]. In this regard, when an ion selective membrane is incorporated, possibly the Li/polyiodide battery performance can be efficiently improved by localizing those polyiodide anions within the cathode side by the electrostatic repulsion effect.

Motivated by this issue, we designed and fabricated a proof-of-concept rechargeable lithium/polyiodide (Li/PI) semi-liquid battery with a Nafion-functionalized composite membrane for the ion selective Li/PI configuration. After a lithiation process, the penetrated Nafion in the porous membrane enabled the transport of Li^+ ions while mitigating the diffusion of polyiodide anions to the anode side due to the electrostatic repulsion between the negatively charged perfluorinated functional groups and polyiodide anions. Consequently, the cycling stability of Li/PI batteries with such a Nafion-functionalized composite membrane was dramatically improved, with a cycle decay rate below 0.16% for over 100 cycles at 0.2 C.

2. Experimental

2.1. Material preparation

The polyiodide (LiI_3) solution was prepared by dissolving a desired amount of stoichiometric I_2 and LiI in 1,3-dioxolane (DOL)/1,2-dimethoxyethane (DME) solution (1:1 in volume) with the addition of 1 M LiTFSI and 1 wt% $LiNO_3$ additive (~0.15 M). For the typical preparation of 1 M LiI_3 solution, 1.27 g of elemental I_2 and 0.67 g of LiI were added to 5 mL of DOL/DME (1:1) based electrolyte. The obtained suspension was stirred for 1 h to yield a red-brown LiI_3 solution.

Polypropylene membranes (Celgard 2500, porosity 55%, 1.40 mg cm^{-2}) were coated with the Nafion solution (1 wt% in dimethylformamide (DMF) solution) and dried on a hotplate at 80 °C afterward. The Nafion amounts were varied from 0.8, 1.2 and 1.6 mg cm^{-2}. To lithiate the as-prepared membranes, the membranes were soaked in the blank electrolyte comprising 1.0 M LITFSI and 0.15 M $LiNO_3$ in the DME/DOL (1:1, v/v) solvent for a week [38]. The Celgard separator coated with the lithiated Nafion, which was denoted as the Nafion-functionalized composite membrane, was then used for the battery assembly without any further treatment.

2.2. Cell assembly and test

One piece of lithium (16 mm diameter) was placed onto the bottom of the copper cell body, a layer of Celgard separator or Nafion-functionalized composite membrane (18 mm diameter) was placed onto the lithium foil, followed by the placement of a piece of carbon cloth (12 mm diameter, hydrophilic). As previously reported in the literature, the overhang method, namely using an electrode with a smaller size than the Li anode, can decrease the dendrite growth [32]. Herein, a circular carbon cloth with a smaller diameter (12 mm) was exploited and 25 μL as-prepared catholyte containing LiI_3 with various concentrations (0.33 M, 1 M and 1.5 M) were injected into batteries without further addition of blank electrolyte. The theoretical capacities (I_2/I^-) for three groups of batteries were determined as 0.67, 2.0 and 3.0 mAh respectively. To avoid the unexpected iodine precipitation, the batteries were cycled in a voltage range of 2–3.4 V.

The electrochemical measurements were determined with a potentiostat (Princeton Applied Research, PARSTAT M2273). Electrochemical impedance spectroscopy (EIS) measurement using a frequency range from 100 kHz to 1 Hz with a wave amplitude of 5 mV was applied to the assembled Li/PI batteries after charge. Besides, the cyclic voltammetry (CV) of the assembled Li/PI batteries was tested at a scanning rate of 0.5 mV s^{-1} with the carbon cloth electrode as the working electrode and lithium coil as both reference and counter electrodes.

The visible permeability test to examine the properties of the membranes was carried out in an H-type glass cell. The assembly of

transparent battery was conducted in a glove box to exclude the influence of moisture and oxygen. Routine Celgard 2500 and Nafion-functionalized composite membranes were inserted in the glass cell respectively. Carbon cloth was set in the cathode chamber with the addition of 15 mL 25 mM LiI solution with a theoretical capacity of 10.0 mAh ($LiI \rightarrow I_2$), while lithium foil was set in the anode chamber with the addition of 15 mL blank electrolyte. During the test, the visible cell was charged at 1.0 mA cm^{-2} to generate the polyiodide solution and the transport behavior of polyiodide across the membrane was recorded.

2.3. Material characterization

The charged anodes after cycling were washed by pure DME and then dried before SEM observation. A field emission scanning electron microscope (FESEM, JEOL 6700) was used to determine the morphology of the charged anodes with an acceleration voltage of 5 kV. Fourier transform infrared spectroscopy (FTIR) measurements were recorded using Vertex 70 Hyperion 1000 (Bruker) with the assisstance of attenuated total reflectance (ATR) accessories. The absorption spectra were recorded from 1800 cm^{-1} to 400 cm^{-1} with a resolution of 4 cm^{-1}.

3. Results and discussion

3.1. Battery configuration and material characterization

As mentioned, the battery configuration of a Li/PI battery consists of a carbon cloth cathode, a metallic lithium anode, and a separator, all of which are immersed in the ether-based electrolyte. In most cases, the separator is a porous membrane without functional groups (e.g. polypropylene (PP), polyethylene (PE), glass fibers), which has pores in submicron dimension and serves solely as an electronic insulator, allowing polyiodide and iodide anions to freely diffuse through the membranes. As the polyiodide anions can react with metallic lithium under room temperature to generate iodide anions, the lithium anode might be considerably degraded during the cycling process. To address this issue, we explore the idea of CEMs, in which the functional groups are negatively charged. To provide the proof-of-the-concept, Nafion as a typical CEM is exploited, and the negatively charged perfluorinated functional groups repulse the polyiodide anions as illustrated in Fig. 1a and b.

Though promising, the commercial Nafion membrane shows a swelling behavior in the organic ether based solvent, leading to a lower mechanical strength and a considerable deformation when compressed [39]. Thus, instead of using a commercial Nafion membrane, we impregnated the Nafion into the pores of the robust Celgard separator for three folds of benefits: (i) there is minor volume change when soaking in organic solvent; (ii) a lower Nafion loading; (iii) a higher ionic conductivity. As shown in Fig. 2a, it is found that an optimal Nafion loading was achieved at 1.2 mg cm^{-2} for the Nafion-functionalized composite membrane in terms of the battery's discharge capacity. The coulombic efficiency increases at a higher Nafion loading, however the enlarged ionic transportation resistance lowers the active material utilization. That is why the commercial Nafion membrane, even the thinnest Nafion 211 with a Nafion loading of 5 mg cm^{-2}, might not be suitable for use in this case. This message can be further confirmed in the EIS analysis as shown in Fig. S1, where the high-frequency intercept is attributed to the battery's ohmic resistance and the diameter of the semi-circle is attributed to the interfacial and charge transfer resistances of the liquid cathode [8,28]. As shown in Fig. 2b, the battery with a Nafion loading of 1.2 mg cm^{-2} exhibits an ohmic resistance of 19.9 Ω, in comparison, for the battery with a routine separator, the ohmic resistance is 7.1 Ω. As Nafion coated on the separator surface will be in close contact with the carbon cloth cathode, interfacial resistance can be increased as well, which can be attributed to the enlarged interfacial and charge transfer resistances with an increase in Nafion loading.

Fig. 2c shows the ATR-FTIR results of the Nafion membranes with and without the lithiation process. A concerted shifts observed for the peaks at 1710 cm^{-1} to 1640 cm^{-1} when the counter protons are replaced by the Li^+ ions, which is consistent with the lithiation characteristics in the previous relevant studies [34,35,38,40]. A prelithiation process should be more desirable for improving the battery's performance especially at a higher current density as can be found in Fig. S2. Fig. 2(d–f) compare the SEM morphologies of the lithiated Nafion membrane and the commercial Celgard separator (PP/PE). The routine Celgard separator shows a porous structure with pore dimensions in the submicron scale, which unavoidably allows the migration of the dissolved lithium polyiodide/iodide species between the cathode and the anode. As shown in Fig. 2e, most of the submicron pores have been filled after the infiltrated Nafion loading reaches 0.8 mg cm^{-2}, but it is still not sufficient to cover the entire surface of the separator. When the loading is further increased to 1.2 mg cm^{-2}, a compact film is observed to cover the surface, demonstrating a dense and uniform morphology. However, there will be very slight morphology change when the loading is further increased to 1.6 mg cm^{-2}, despite the increase in thickness as can be speculated, which can be confirmed by the cross sectional view of the as-prepared membranes in Fig. S3. Combining electrochemical performance and morphology characterization, it is reasoned that an optimal Nafion loading exists to form a compact thin film to cover onto the porous separator's surface.

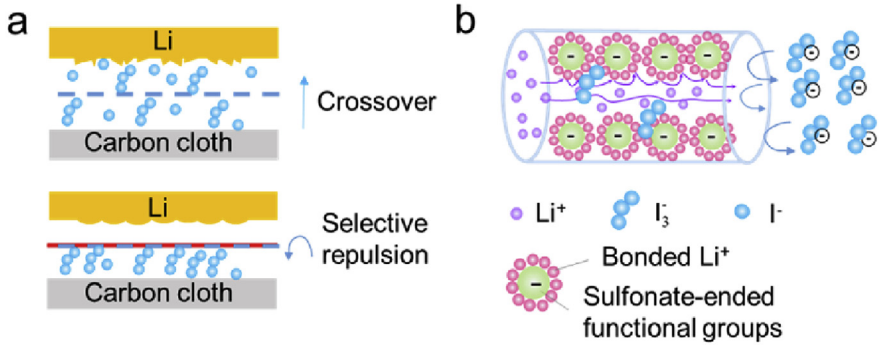

Fig. 1. (a) The schematic illustration of the Li/PI batteries without and with an ion selective membrane. (b) Enlarged schematic for the selective repulsion of polyiodide anions with the use of ion selective membrane (Nafion-functionalized composite membrane).

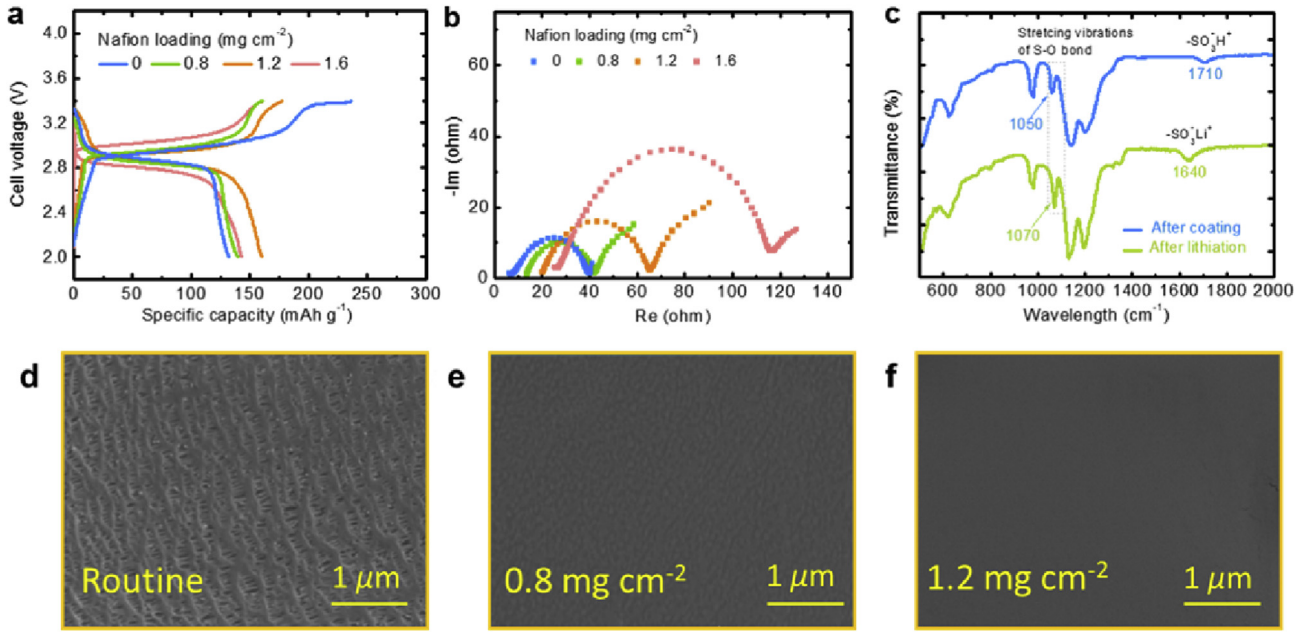

Fig. 2. (a) Charge-discharge curves of Li/PI batteries at 0.6 C using Nafion-functionalized composite membranes with different Nafion loadings (25 μL 0.33 M LiI_3 catholyte was added as the active material). The C rate is calculated based on the specific capacity of elemental iodine (211 mAh g^{-1}). (b) EIS (electrochemical impedance spectroscopy) results of the assembled batteries with different Nafion loadings; (c) FTIR spectra of Nafion-functionalized composite membranes without and with the lithiation process; (d–f) the top view of the routine separator and Nafion-functionalized composite membranes.

In addition to the Nafion loading on the membrane, we herein discuss the effect of catholyte concentration. Because the increase of catholyte concentration renders a higher concentration gradient for the polyiodide crossover, to identify whether the introduction of a Nafion-functionalized composite membrane can sustain in the concentrated catholyte, the performance was tested at 0.33, 1 and1.5 M LiI_3. It is found that at a relatively low catholyte concentration, the volumetric capacity can be prolonged, achieving a value slightly exceeding the theoretical capacity of I_3^-/I^- redox couple (e.g. 17.9 Ah L^{-1} for 0.33 M LiI_3 catholyte). It can be seen from the cyclic voltammetry profile in Fig. S4 that there exist two separated anodic peaks representing transformation of I^-/I_3^- (2.78–3.35 V) and I_3^-/I_2 (3.35–3.60 V), respectively. Also, from the galvanostatic curve at the window voltage of 2–3.6 V (Fig. S5), two voltage plateaus can be observed, where the higher voltage plateau represents the redox reaction of I_3^-/I_2 and the lower voltage plateau mostly represents the redox reaction of I^-/I_3^- in consistence with the CV result. Interestingly, it is found that the lower voltage plateau is longer than the two times of the higher voltage plateau, indicating that the redox reaction of I_3^-/I_2 occurs at the lower voltage plateau as well. Based on these result, at a cut-off charge voltage of 3.4 V, I_3^- can be partially oxidized into I_2 and contributes a portion of the discharge capacity. It is worthwhile noting that the solubility of elemental iodine is intrinsically low (0.60 ± 0.05 M I_2, 298 K). Hence, a narrow voltage window is desirable if the battery is intended to be operated in a cathode-flow mode with a higher iodide concentration.

When the batteries are cycled at the same rate (1 C), a higher catholyte concentration leads to a higher superficial current. In this regard, the lower catholyte utilization ratio at a higher catholyte concentration can be attributed to the concentration polarization. Herein, at a catholyte concentration of 1.5 M LiI_3, a catholyte volumetric energy density of 170.5 Wh L^{-1} (60.5 Ah L^{-1}) was achieved. With the increase of catholyte concentration, the overall polyiodide crossover amount becomes larger and the side reactions ($2Li + I_3^- \rightarrow 2Li^+ + 3I^-$ or $I_3^- + 2e^- \rightarrow 3I^-$) on the Li anode will be promoted, that is why a slight decrease in coulombic efficiency was found at a higher catholyte concentration (Fig. 3b). Even so, reasonably high energy efficiency (>80%) could be still achieved and the discharge capacities of the as-prepared batteries were well maintained over 10 cycles as shown in Fig. S6 with minor decay. The achieved catholyte volumetric energy density is almost 5 times higher than the all vanadium redox flow batteries do [41]. Also, it should be noted that this value is comparable to the highest reported volumetric energy density for Zn-I_2 flow batteries with an iodide concentration of 10 M [32]. In the next section, the rate and long-term cycling performance of the batteries will be further investigated, for a compromise between the catholyte utilization ratio (specific capacity) and the energy density, an intermediate concentrated catholyte (1 M LiI_3) will be adopted.

3.2. Electrochemical performance

In this section, we further demonstrate the rate and cycling performances of the as-prepared batteries. As presented in Fig. 4a, batteries with the routine separator and Nafion-functionalized composite membrane were operated from 0.2 to 2 C. With a routine separator, the Li anode is exposed to the corrosive electrolyte containing polyiodide and the battery suffers from rapid capacity decay as well as a very low coulombic efficiency (~40% for the initial cycle at 0.2 C), as can be seen from the first several cycles in Fig. 4b. In sharp contrast, under the introduction of a Nafion-functionalized composite membrane, the resultant battery demonstrated dramatically improved stability as well as excellent capacity retention. The representative charge/discharge profiles at the 5th cycle at different rates are displayed in Fig. 4c. The discharge capacity only decreases for ~20%, from 0.2 C to 2 C, implying the fast kinetics of I_3^-/I^- redox couple. Moreover, with an increase of discharge rate, it is found that the coulombic efficiency dramatically increases, indicating that when the discharge time is shortened, the overall crossover amount can be efficiently diminished [42]. This is why Fig. 4a and c show that the coulombic efficiency

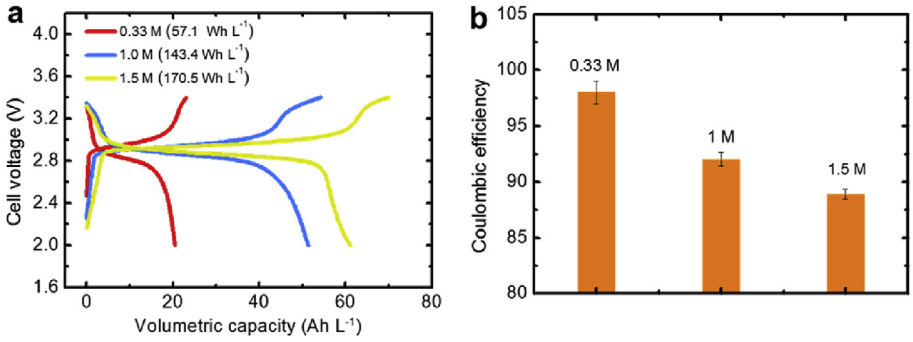

Fig. 3. (a) Charge-discharge curves at different catholyte concentrations (0.33, 1 and 1.5 M LiI_3) at 1 C for the Li/PI batteries with the Nafion-functionalized composite membrane (Nafion loading 1.2 mg cm^{-2}); (b) the corresponding effect of catholyte concentration on coulombic efficiency. The volumetric capacity is calculated based on the volume of catholyte volume (25 μL).

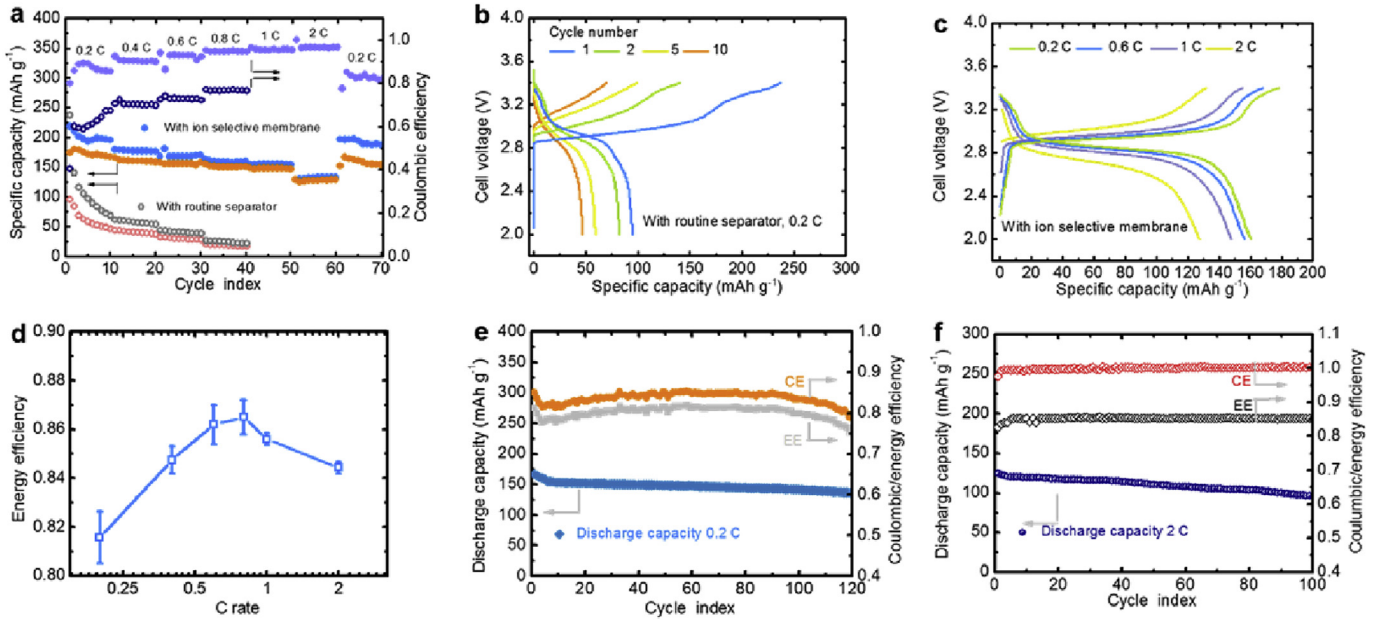

Fig. 4. (a) Comparison of rate performance of Li/PI batteries with a routine separator and a Nafion-functionalized composite membrane (Nafion loading 1.2 mg cm^{-2}) using 1 M LiI_3 cathoyte; (b) voltage profile of the Li/PI battery with a routine separator; (c) voltage profile of the Li/PI battery with a Nafion-functionalized composite membrane (ion selective Li/PI battery); (d) the effect of C rate on the ion selective Li/PI battery's energy efficiency; (e) cycling performance of the ion selective Li/PI battery at 0.2 C; (f) cycling performance of the ion selective Li/PI battery at 2 C. The C rate is calculated based on the specific capacity of elemental iodine (211 mAh g^{-1}).

(CE) increases at a higher current density. On the other hand, at a higher current density, the polarization will be increased, lowering the voltage efficiency (VE). As the energy efficiency is the product of coulombic and voltage efficiencies (EE = CE × VE), an optimum in the energy efficiency will exist at a particular current density as shown in Fig. 4d.

To evaluate the long-term cycling performance, the Li/PI batteries were cycled at 0.2 C and 2 C respectively as shown in Fig. 4e and f. Stable cycling performances were achieved for both situations, suggesting that the batteries show excellent reversibility at higher rates and cycling stability at lower rates. Though the coulombic efficiency for 0.2 C cycling was relatively low (80%–85%), the discharge capacity did not undergo a visible drop. It is thereby speculated that the self-discharge behavior might occur in an electrochemical approach: $I_3^- + 2e^- \rightarrow 3I^-$, which induces minor change on the Li anode surface.

With these results, we compared the proposed Li/PI systems with Li-ion batteries and other Li based semi-liquid systems. It is found that iodine as an active material inherently shows its advantage in terms of its gravimetric/volumetric energy density if compared with the existing cathode material such as $LiCoO_2$, $LiMn_2O_4$ and $LiFePO_4$ as can be seen in Fig. S7. On the other hand, in terms of the catholyte volumetric energy density, with the high solubility of active material, the Li/PI system is also more superior to the reported Li/polysulfide, Li/ferrocene and Li/TEMPO systems as can be found in Table S1 [15,43,44]. Also, with the Nafion-functionalized composite membrane the ion-selective Li/PI system demonstrates reasonably high coulombic and energy efficiencies. We also demonstrated that this type of Nafion-functionalized composite membrane was effective for other Li-halide semi-liquid battery systems [25,45]. When applied in a semi-liquid battery with polybromide as catholyte, stable cycling can be demonstrated as well (Figs. S8 and S9).

3.3. Electrochemical stability

Anode characterization was further exploited to examine whether the metallic lithium can be protected after long-term

cycling. Fig. 5(a–c) show the surface morphologies of the routine and cycled lithium anodes taken out of the batteries either with the routine separator or with the Nafion-functionalized composite membrane. In comparison to the fresh Li metal, for the one in the battery with a routine separator, the surface of the lithium anode becomes highly porous over cycling due to the corrosion of polyiodide shuttle. In sharp contrast, as shown in Fig. 5c, formation of lithium dendrite can be clearly observed for the battery protected by the Nafion-functionalized composite membrane after 50 cycles, in well consistence with the reported results [46]. As shown in the inset in Fig. 5c, after 120 cycles at 0.2 C, the dendrites become more protruding. The obtained results suggest that the lithium electrodeposition process has not been seriously affected by the corrosion of polyiodide shuttle and anode engineering tactics to address the lithium dendrite issue should be desirable for further research.

Electrochemical impedance spectroscopy results have further confirmed the above message. As presented in Fig. 5d, the semicircle at the middle-frequency region (R_{SEI} and R_{ct}) is significantly enlarged after 5 cycles for the battery with the routine separator, which should be attributed to the increasingly non-uniform passivation layer. In contrast, only slight change of middle-frequency region is found for the case with the Nafion-functionalized composite membrane even after 120 cycles. Due to the high solubility of LiI and LiI_3 in ether-based solvents, there might not exist considerable active material loss during cycling. In this regard, we reason that one of the major attributes for capacity decay is the degradation of the lithium anode and the enlarged impedances [32,33,47–51].

In addition to the anode characterization, direct observation of the crossover phenomena helps to evaluate the stability of the battery system. As shown in Fig. 6a, we used a visible H-cell to simulate the charge process of the Li/PI battery. Specifically, we focus on the charging process, as the infinite charging induced by the shuttle effect is a critical issue facing Li/PI battery. Blank electrolyte and 15 mL 25 mM LiI solution with a theoretical capacity of 10.0 mAh ($LiI \rightarrow I_2$) were added into the anode and cathode chambers respectively. The visible cell was charged with a rate of 1.2 mA, after every 1 h charge duration the battery was rested for 5 min to allow for the redistribution of polyiodide species. As can be seen in Fig. 6b, the cell voltage linearly climbed up over the charge process attaining a charge capacity of ~6.0 mAh, indicating that LiI in the cathode chamber has been mostly converted to LiI_3. Meanwhile. during the charge process, polyiodide with a red-brown color was continuously generated around the carbon cloth electrode and the polyiodide concentration can be visibly found to increase. With the incorporation of Nafion-functionalized composite membrane, polyiodides could be well accommodated within the cathode side, only slight color change in the anode chamber could be observed for a duration of 5 h. Also, for a storage time of 8 h, there was no obvious color change in the anode side. In contrast, when we replaced the Nafion-functionalized composite membrane with the routine separator, it was found that the polyiodide crossover occurred in a very rapid manner, for the duration of less than 1 h, the polyiodide species had migrated from the cathode to the anode chamber, which was confirmed by the cell voltages during storage shown in Fig. 6c. Under the same storage time, induced by self-discharge, the battery with a routine separator showed a much faster cell voltage drop. Therefore, the achieved results clearly indicate that the membrane performs a substantial role to shield the Li anode from the polyiodide shuttle attack.

4. Conclusion

In summary, the Nafion-functionalized composite membrane

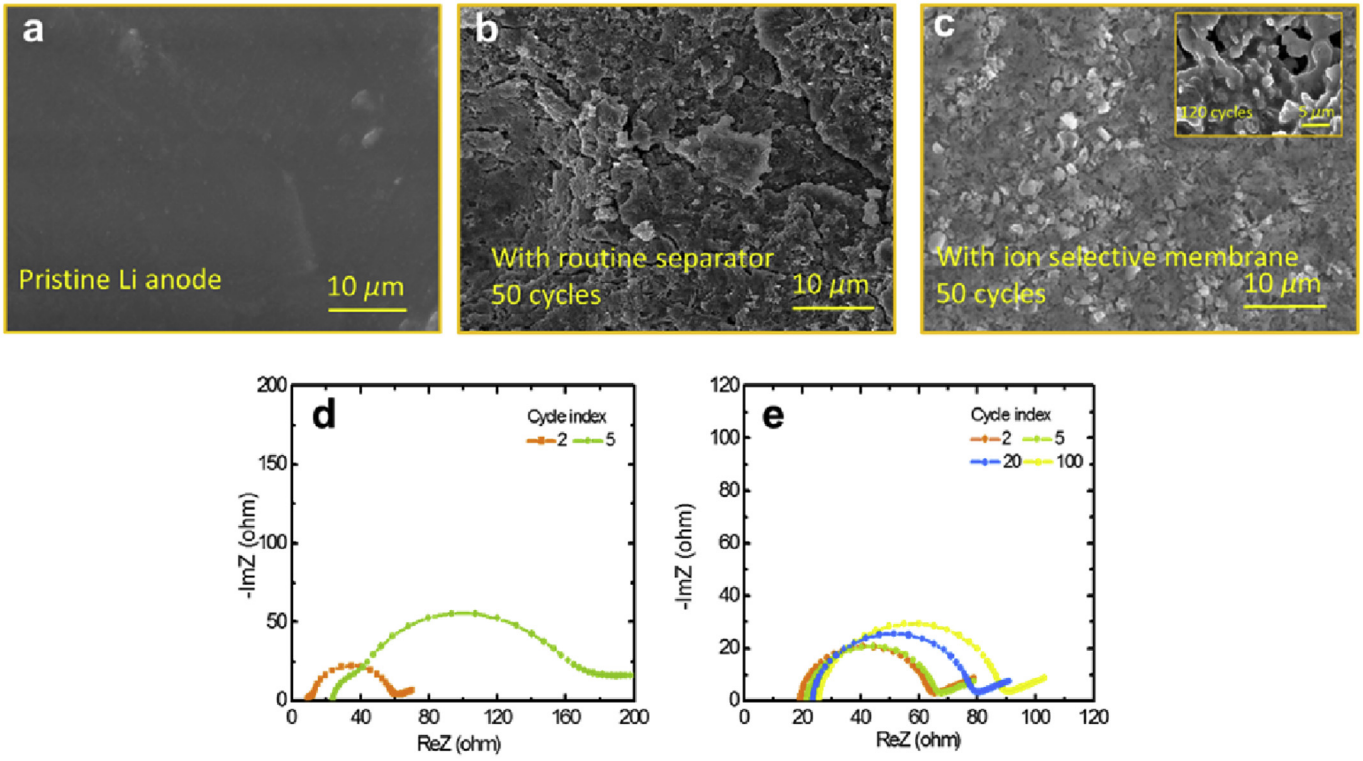

Fig. 5. (a) Pristine metallic lithium anode; (b) Li anode in the Li/PI battery with a routine separator after 50 cycles; (c) Li anode in the Li/PI battery with a Nafion-functionalized composite membrane (Nafion loading 1.2 mg cm^{-2}) after 50 cycles, the inset shows the Li anode after 120 cycles; (d, e) EIS results after charge: (d) the Li/PI battery with a routine separator; (e) the Li/PI battery with a Nafion-functionalized composite membrane.

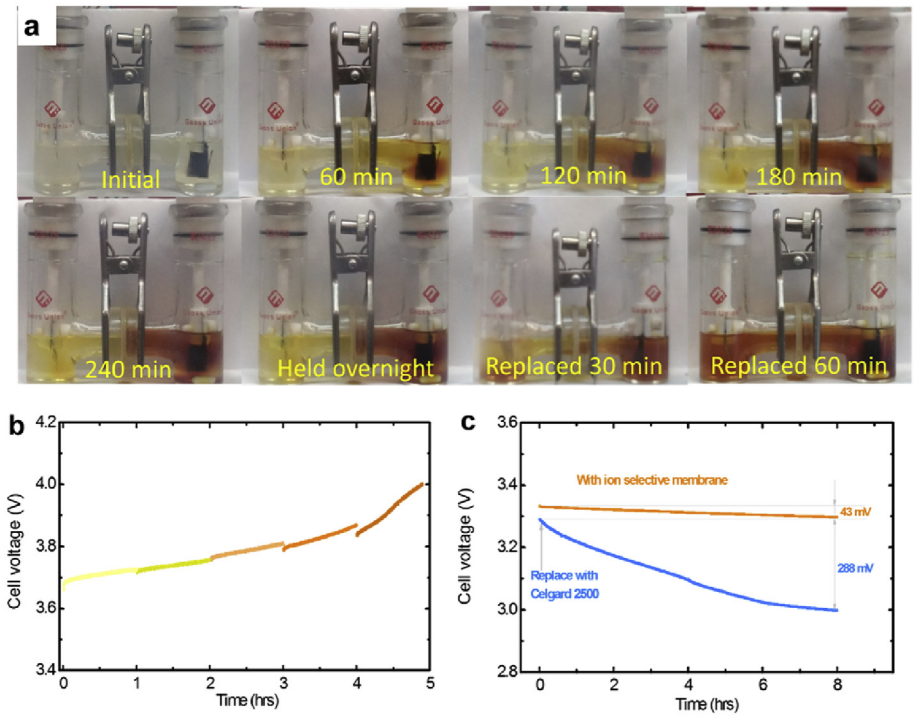

Fig. 6. (a) The optical images for the generation and diffusion of polyiodide during the charge process, initially a Nafion-functionalized composite membrane was exploited and the battery was charged for 5 h. After being held overnight, the electrolytes were extracted and the Nafion-functionalized composite membrane was replaced by a routine Celgard 2500 separator. (b) The charge profile for the transparent battery with the Nafion-functionalized composite membrane. (c) After charge, the transparent battery's resting voltage.

was exploited for semi-liquid Li/polyiodide batteries, which allowed the free transportation of lithium cations and suppression of polyiodide shuttle due to the electrostatic interactions. The resultant batteries showed a greatly improved cycling stability with a capacity decay of 0.16% per cycle for over 100 cycles, indicating that the use of the Nafion-functionalized composite membrane is highly effective in building a complete anion shield. With these results, we envisage that the shuttle effect could be overcome in the aprotic Li/polyiodide battery configuration, which offers promising opportunities for Li based flow battery research.

Acknowledgment

Y.X. Ren and M. Liu contributed equally to this work. The work was fully supported by Research Grants Council of the Hong Kong Special Administrative Region, China (Project No. 16213414).

Appendix A. Supplementary data

Supplementary data related to this article can be found at http://dx.doi.org/10.1016/j.jpowsour.2016.12.043.

References

[1] Z. Yang, J. Zhang, M.C.W. Kintner-Meyer, X. Lu, D. Choi, J.P. Lemmon, J. Liu, Chem. Rev. 111 (2011) 3577–3613.
[2] M. Armand, J.M. Tarascon, Nature 451 (2008) 652–657.
[3] B. Dunn, H. Kamath, J.M. Tarascon, Science 334 (2011) 928–935.
[4] M.S. Islam, C.A.J. Fisher, Chem. Soc. Rev. 43 (2014) 185–204.
[5] J. Chen, F. Cheng, Accounts Chem. Res. 42 (2009) 713–723.
[6] Y.X. Ren, T.S. Zhao, P. Tan, Z.H. Wei, X.L. Zhou, Appl. Energy 187 (2017) 706–716.
[7] Y. Ren, T. Zhao, M. Liu, P. Tan, Y. Zeng, J. Power Sources 336 (2016) 115–125.
[8] M. Liu, D. Zhou, Y.-B. He, Y. Fu, X. Qin, C. Miao, H. Du, B. Li, Q.-H. Yang, Z. Lin, Nano Energy 22 (2016) 278–289.
[9] M. Liu, H. Jiang, Y. Ren, D. Zhou, F. Kang, T. Zhao, Electrochim. Acta 213 (2016) 871–878.
[10] M. Liu, D. Zhou, H. Jiang, Y. Ren, F. Kang, T. Zhao, Nano Energy 28 (2016) 97–105.
[11] P. Bai, J. Li, F.R. Brushett, M.Z. Bazant, Energy Environ. Sci. 9 (2016) 3221–3229.
[12] H. Jiang, Z. Lu, M. Wu, F. Ciucci, T. Zhao, Nano Energy 23 (2016) 97–104.
[13] Y. Yang, G. Zheng, Y. Cui, Energy Environ. Sci. 6 (2013) 1552–1558.
[14] X. Wei, W. Xu, M. Vijayakumar, L. Cosimbescu, T. Liu, V. Sprenkle, W. Wang, Adv. Mater. 26 (2014) 7649–7653.
[15] Y. Ding, Y. Zhao, G. Yu, Nano Lett. 15 (2015) 4108–4113.
[16] P. Bai, M.Z. Bazant, Nat. Commun. 5 (2014).
[17] Y. Lu, J.B. Goodenough, J. Mater. Chem. 21 (2011) 10113–10117.
[18] Y. Lu, J.B. Goodenough, Y. Kim, J. Am. Chem. Soc. 133 (2011) 5756–5759.
[19] Y. Zhao, M. Hong, N. Bonnet Mercier, G. Yu, H.C. Choi, H.R. Byon, Nano Lett. 14 (2014) 1085–1092.
[20] Y. Zhao, Y. Ding, Y. Li, L. Peng, H.R. Byon, J.B. Goodenough, G. Yu, Chem. Soc. Rev. 44 (2015) 7968–7996.
[21] Y. Zhao, H.R. Byon, Adv. Energy Mater. 3 (2013) 1630–1635.
[22] Y. Zhao, L. Wang, H.R. Byon, Nat. Commun. 4 (2013).
[23] Y. Zhao, Y. Ding, J. Song, L. Peng, J.B. Goodenough, G. Yu, Energy Environ. Sci. 7 (2014) 1990–1995.
[24] H. Pan, X. Wei, W.A. Henderson, Y. Shao, J. Chen, P. Bhattacharya, J. Xiao, J. Liu, Adv. Energy Mater. 5 (2015).
[25] P. Bai, M.Z. Bazant, Electrochim. Acta 202 (2016) 216–223.
[26] H. Chen, Y.C. Lu, Adv. Energy Mater. 6 (2016).
[27] Y.L. Wang, Q.L. Sun, Q.Q. Zhao, J.S. Cao, S.H. Ye, Energy Environ. Sci. 4 (2011) 3947–3950.
[28] Q. Zhao, Y. Lu, Z. Zhu, Z. Tao, J. Chen, Nano Lett. 15 (2015) 5982–5987.
[29] S. Evers, T. Yim, L.F. Nazar, J. Phys. Chem. C 116 (2012) 19653–19658.
[30] S.S. Zhang, Electrochim. Acta 70 (2012) 344–348.
[31] Z. Liang, G. Zheng, C. Liu, N. Liu, W. Li, K. Yan, H. Yao, P.-C. Hsu, S. Chu, Y. Cui, Nano Lett. 15 (2015) 2910–2916.
[32] Z. Li, J. Huang, B.Y. Liaw, V. Metzler, J. Zhang, J. Power Sources 254 (2014) 168–182.
[33] X.B. Cheng, R. Zhang, C.Z. Zhao, F. Wei, J.G. Zhang, Q. Zhang, Adv. Science (2015).
[34] K.A. Mauritz, R.B. Moore, Chem. Rev. 104 (2004) 4535–4585.
[35] H.Y. Liang, X.P. Qiu, S.C. Zhang, W.T. Zhu, L.Q. Chen, J. Appl. Electrochem. 34 (2004) 1211–1214.
[36] Y. Lei, B. Zhang, B. Bai, T.S. Zhao, J. Power Sources 299 (2015) 202–211.
[37] X.-G. Yang, Q. Ye, P. Cheng, T.S. Zhao, Appl. Energy 145 (2015) 306–319.
[38] X. Yu, J. Joseph, A. Manthiram, J. Mater. Chem. A 3 (2015) 15683–15691.
[39] Z. Cai, Y. Liu, S. Liu, L. Li, Y. Zhang, Energy Environ. Sci. 5 (2012) 5690–5693.
[40] I. Bauer, S. Thieme, J. Brückner, H. Althues, S. Kaskel, J. Power Sources 251 (2014) 417–422.

[41] Y. Zeng, T. Zhao, L. An, X. Zhou, L. Wei, J. Power Sources 300 (2015) 438–443.
[42] Y.V. Mikhaylik, J.R. Akridge, J. Electrochem. Soc. 151 (2004) A1969–A1976.
[43] X. Wei, W. Xu, M. Vijayakumar, L. Cosimbescu, T. Liu, V. Sprenkle, W. Wang, Adv. Mater. 26 (2014) 7649–7653.
[44] Y. Yang, G. Zheng, Y. Cui, Energy Environ. Sci. 6 (2013) 1552–1558.
[45] P. Bai, V. Viswanathan, M.Z. Bazant, J. Mater. Chem. A 3 (2015) 14165–14172.
[46] W. Li, H. Yao, K. Yan, G. Zheng, Z. Liang, Y.-M. Chiang, Y. Cui, Nat. Commun. 6 (2015).
[47] D. Aurbach, E. Zinigrad, H. Teller, P. Dan, J. Electrochem. Soc. 147 (2000) 1274–1279.
[48] W. Xu, J. Wang, F. Ding, X. Chen, E. Nasybulin, Y. Zhang, J.G. Zhang, Energy Environ. Sci. 7 (2014) 513–537.
[49] H. Kim, G. Jeong, Y.U. Kim, J.H. Kim, C.M. Park, H.J. Sohn, Chem. Soc. Rev. 42 (2013) 9011–9034.
[50] G. Zheng, S.W. Lee, Z. Liang, H.W. Lee, K. Yan, H. Yao, H. Wang, W. Li, S. Chu, Y. Cui, Nat. Nanotechnol. 9 (2014) 618–623.
[51] X.B. Cheng, T.Z. Hou, R. Zhang, H.J. Peng, C.Z. Zhao, J.Q. Huang, Q. Zhang, Adv. Mater. 28 (2016) 2888–2895.

Journal of Power Sources 327 (2016) 258–264

Contents lists available at ScienceDirect

Journal of Power Sources

journal homepage: www.elsevier.com/locate/jpowsour

Performance enhancement of iron-chromium redox flow batteries by employing interdigitated flow fields

Y.K. Zeng [a], X.L. Zhou [a], L. Zeng [a, b], X.H. Yan [a], T.S. Zhao [a, *]

[a] Department of Mechanical and Aerospace Engineering, The Hong Kong University of Science and Technology, Clear Water Bay, Kowloon, Hong Kong, China
[b] HKUST Jockey Club Institute for Advanced Study, The Hong Kong University of Science and Technology, Clear Water Bay, Kowloon, Hong Kong SAR, China

HIGHLIGHTS

- The ICRFBs with the interdigitated and serpentine flow fields are investigated.
- The IFF design enhances species transport in the porous electrode.
- The IFF design enables more uniform catalyst distribution in the porous electrode.
- The energy efficiency of the ICRFB with the IFF reaches 80.7% at 320 mA cm^{-2}.

ARTICLE INFO

Article history:
Received 30 March 2016
Received in revised form
18 July 2016
Accepted 19 July 2016
Available online 25 July 2016

Keywords:
Flow batteries
Iron-chromium redox flow batteries
Interdigitated flow field
Mass transport
Energy storage

ABSTRACT

The catalyst for the negative electrode of iron-chromium redox flow batteries (ICRFBs) is commonly prepared by adding a small amount of Bi^{3+} ions in the electrolyte and synchronously electrodepositing metallic particles onto the electrode surface at the beginning of charge process. Achieving a uniform catalyst distribution in the porous electrode, which is closely related to the flow field design, is critically important to improve the ICRFB performance. In this work, the effects of flow field designs on catalyst electrodeposition and battery performance are investigated. It is found that compared to the serpentine flow field (SFF) design, the interdigitated flow field (IFF) forces the electrolyte through the porous electrode between the neighboring channels and enhances species transport during the processes of both the catalyst electrodeposition and iron/chromium redox reactions, thus enabling a more uniform catalyst distribution and higher mass transport limitation. It is further demonstrated that the energy efficiency of the ICRFB with the IFF reaches 80.7% at a high current density (320 mA cm^{-2}), which is 8.2% higher than that of the ICRFB with the SFF. With such a high performance and intrinsically low-cost active materials, the ICRFB with the IFF offers a great promise for large-scale energy storage.

1. Introduction

Deployment of intermittent renewable energy sources such as wind and solar energy has been increasing substantially, which raises an urgent demand to develop the large-scale energy storage devices for continuous and reliable power output [1–3]. The redox flow battery (RFB) has attracted extensive interests as a promising large-scale energy storage technology due to its unique advantages including ease of scalability, long cycle life, intrinsic safety and high efficiency [3]. In the past decades, various RFB systems have been proposed and developed [3–16]. However, the current RFB technologies still have not met the stringent cost and performance requirements for the broad penetration of energy storage market.

The iron-chromium redox flow battery (ICRFB) utilizes the low-cost and benign Fe(II)/Fe(III) and Cr(II)/Cr(III) redox couples in the acid supporting medium as the catholyte and anolyte, respectively [2,17]. The cost of chromium and iron active materials used in ICRFBs is estimated to be as low as \$17 kWh^{-1}, which provides the ICRFB a sufficient basis and great possibility to be a cost-effective energy storage system [2,17,18].

Historically, the ICRFB adopts a flow-through cell structure, in which the electrolyte is directly pumped through the porous electrode [19]. To bypass high pump loss, the conventional ICRFBs have thick electrodes (generally 3.0–6.0 mm) [20–22], leading to a high ohmic resistance [23,24]. For this reason, the conventional ICRFB is limited to a low operating current density of 80 mA cm^{-2},

* Corresponding author.
E-mail address: metzhao@ust.hk (T.S. Zhao).

http://dx.doi.org/10.1016/j.jpowsour.2016.07.066
0378-7753/

resulting in bulky and costly cell stacks [18,25]. Recently, an ICRFB with the serpentine flow field (SFF) cell structure and carbon paper electrodes enables a high operating current density of 200 mA cm^{-2}, primarily due to a reduced ohmic loss [26].

In addition to the ohmic loss, the activation loss plays an important role in the battery performance, which is closely associated with the active surface area and electrochemical kinetics of redox couples. The Fe(II)/Fe(III) redox couple has an excellent electrochemical kinetics, and its kinetic constant is up to 8.6×10^{-2} cm s^{-1} on the oxidative pretreated pyrographite electrode [27]. The kinetics of the Cr(II)/Cr(III) redox couple is slow on most the carbonaceous electrodes, while the kinetic constant of Cr(II)/Cr(III) redox couple on the electrodeposited Bi catalyst is as high as 1.35×10^{-3} cm s^{-1} [28], which is generally comparable to other redox couples reported in the literature [29]. Moreover, the Bi catalyst has a high overpotential to suppress hydrogen evolution during the reducing process of Cr(III) to Cr(II). However, the Bi catalyst has a relatively low oxidation potential (0.05 V vs. SHE), and tends to be oxidized by air or ferric ions. To avoid this issue, the typical method for catalyst preparation is to add a small amount of Bi^{3+} ions in the electrolyte and synchronously electrodeposit the metallic particles on the electrode at the beginning of charge process [1,25,30]. During the in-situ electrodeposition process, the flow field design has great influence on the mass transport and concentration distribution of Bi^{3+} ions in the porous electrode, and further affects the catalyst distribution, which influences the active surface area and activation loss of the ICRFB. Previous studies have involved the effects of flow field designs on the mass transport characteristics in vanadium redox flow batteries (VRFBs) [22,31–34]. Shohji Tsushima *et al.* found that the VRFB with the interdigitated flow field (IFF) delivered a higher mass transport limitation than that with the SFF due to the enhanced convection of electrolyte in the electrodes [33]. In addition, other studies found that the IFF design has lower pump loss than the SFF design does [31,32].

Unlike the situations in VRFBs, the flow field designs in ICRFBs not only influence the transport and distribution of redox-active ions (Fe and Cr ions) in the porous electrode, but also affect the activation loss, as the Bi catalyst distribution is susceptible to the transport and concentration distribution of Bi^{3+} ions (mM level) during the in-situ catalyst electrodeposition process. In this work, the effects of flow field designs on the catalyst electrodeposition process and battery performance are investigated. It is further found that the energy efficiency of the ICRFB with the IFF reaches 80.7% at a high operating current density of 320 mA cm^{-2}, which is 8.2% higher than that of the ICRFB with the SFF.

2. Experimental

2.1. ICRFB setup

The lab-scale ICRFB with the IFF was designed and fabricated. The carbon papers (SGL, 10AA, 0.4 mm thickness) were pretreated in air at 500 °C for 5 h and served as the electrodes. Both the negative and positive electrodes were made of two layers of carbon papers with active area of 2.0 cm × 2.0 cm, which were separated by the Nafion® NR-212 membrane. The polytetrafluoroethylene gaskets with 0.5 mm thickness were used to give an electrode compression ratio of approximately 40%. The IFFs with the channel depth 1.5 mm, the channel width 1.0 mm and rib width 1.0 mm were machined on the graphite plates. The gold-coated copper current collectors were adjacent to the graphite plates, and were clamped by the aluminum end plates. 20 mL mixed-reactant solutions of 1.0 M $FeCl_2$ (Aladdin) + 1.0 M $CrCl_3$ (Aladdin) + 3.0 M HCl (VWR) + 0.005 M Bi^{3+} (Bi_2O_3: Aladdin) were used as both the anolyte and catholyte. The electrolytes were circulated in the Norprene® #16 Chemical Tubing by a 2-channel peristaltic pump (Longer pump, BT100-1F). The SFF design, one of the most widely used flow field design in fuel cells and flow batteries [9,31,35–39], was used for comparison. For the ICRFB with the SFF, the components such as the channel, rib, electrode, gasket and membrane were identical with the ICRFB with the IFF.

2.2. Test and characterization

The cell tests were conducted on Arbin BT2000 (Arbin® Instrument). The cell and the electrolyte reservoirs were placed in a temperature chamber at 65 °C. For the polarization test, the ICRFBs were charged to approximately 50% state-of-charge (SOC) before the tests. For each current density, the battery discharged for 20 s, rested for 10 s, and charged at the same current density for 20 s to keep the SOC constant during the polarization test. For the charge-discharge tests, the charge cut-off voltage was 1.2 V to mitigate hydrogen evolution, which could occur at the negative electrode during the charge process, and the discharge cut-off voltage was 0.8 V. The flow rate of the electrolyte was 50 mL min^{-1}. The cycle test was conducted at 320 mA cm^{-2} and 65 °C, and 50 mL mixed-reactant solutions of 1.0 M $FeCl_2$ + 1.0 M $CrCl_3$ + 3.0 M

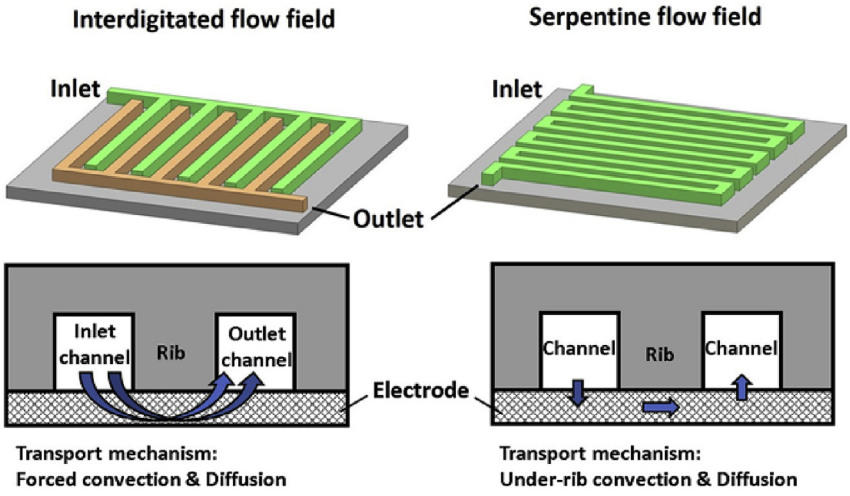

Fig. 1. Schematic of the interdigitated flow field and serpentine flow field.

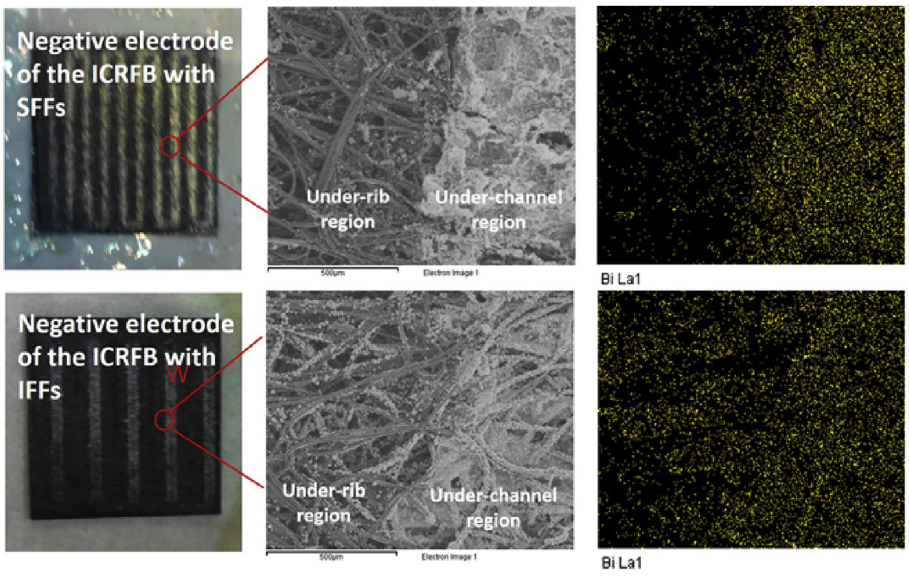

(a)

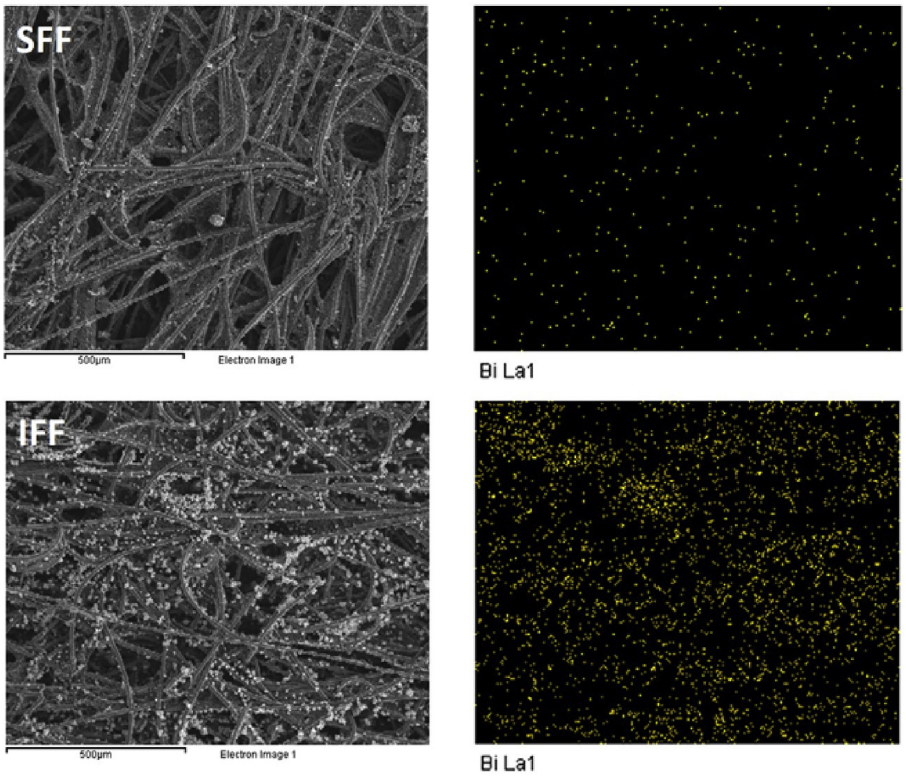

(b)

Fig. 2. SEM images and EDX mappings of (a) the electrodes near the current collector and (b) the electrode near the membrane in the ICRFBs with SFFs and IFFs.

HCl + 0.002 M Bi^{3+} were used as both the anolyte and catholyte. The equivalent current density for feeding the initial electrolyte is 20.1 A cm^{-2}. The electrodes were characterized by a scanning electron microscope (JEOL-6300 SEM) and energy dispersive X-ray spectrum (EDX). The internal resistance of ICRFBs and electrochemical impedance spectroscopy (EIS) were measured by a

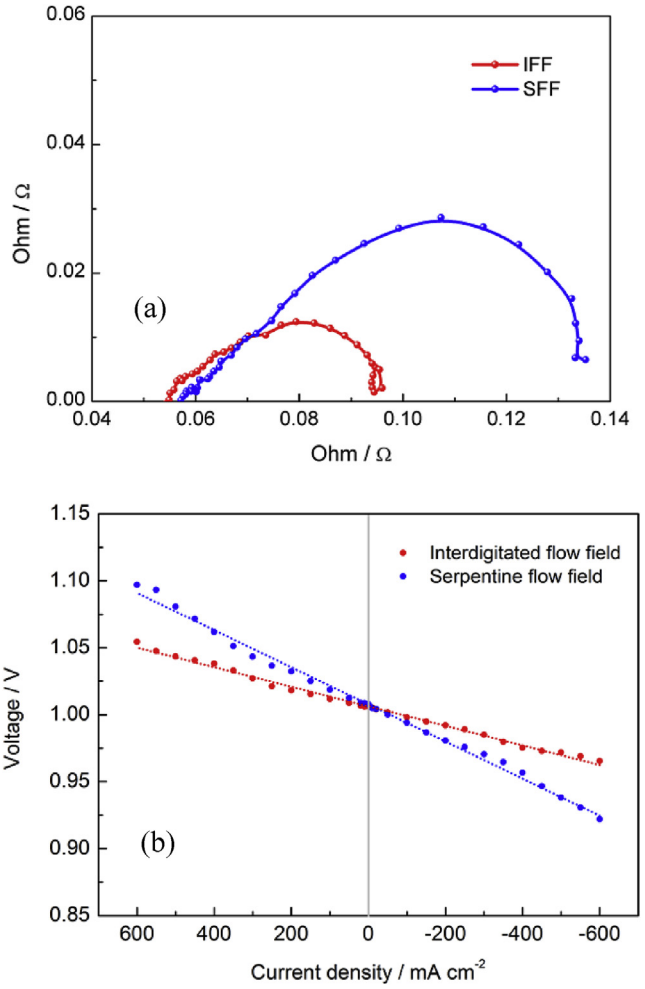

Fig. 3. (a) EIS and (b) IR-free polarization curves of the ICRFBs with IFFs and SFFs.

potentiostat (EG&G Princeton, model M2273) with a frequency range from 100 kHz to 10 mHz.

3. Results and discussion

3.1. In-situ catalyst electrodeposition process

For the Cr(II)/Cr(III) redox reaction, catalysts such as Bi are needed to accelerate the reaction rate and simultaneously suppress the side reaction (hydrogen evolution). The Bi catalyst is electrodeposited on the negative electrode from Bi^{3+} ions (5 mM) in the electrolyte with a current density of 20 mA cm^{-2} at the beginning of charge process. The flow rate of 50 mL min^{-1} initially provides a stoichiometric Bi^{3+} flux of 301.6 mA cm^{-2} (equivalent current density). The electrochemical reactions are as follows:

Positive electrode:

$$Fe^{2+} \xrightarrow{charge} Fe^{3+} + e^- \quad E^0 = +0.77 \text{ V vs. SHE} \tag{1}$$

Negative electrode:

$$Bi^{3+} + 3e^- \xrightarrow{charge} Bi \quad E^0 = +0.05 \text{ V vs. SHE} \tag{2}$$

After the catalyst electrodeposition, the Cr^{3+} ions at the negative electrode are charged to Cr^{2+} ions due to the lower redox potential (−0.41 V vs. SHE). If the catalyst is destroyed during the operation

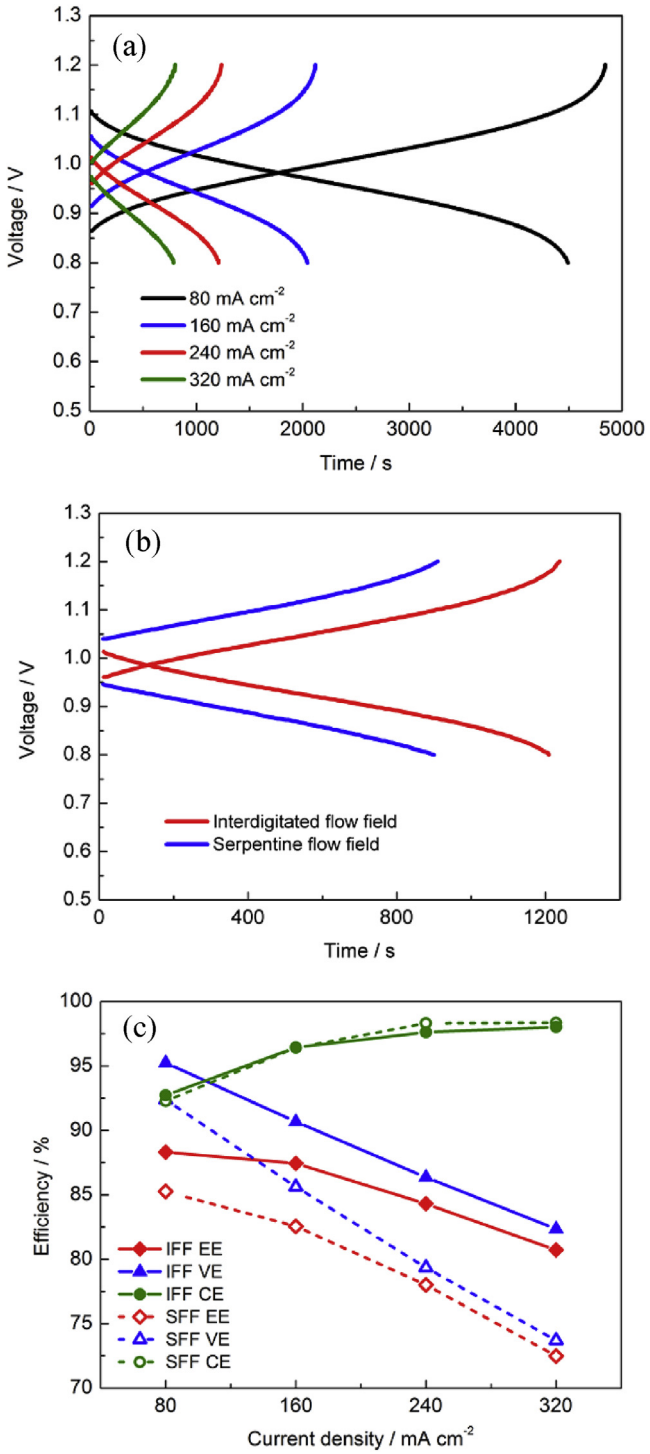

Fig. 4. (a) Charge-discharge curves of the ICRFB with IFFs at various current densities; (b) charge-discharge curves of the ICRFBs with IFFs and SFFs at 240 mA cm^{-2}; and (c) efficiencies of the ICRFBs with IFFs and SFFs.

process of the ICRFB, it can be easily restored by totally stripping and then re-depositing [25].

The flow field serves to distribute active species across the entire electrode, which greatly impacts on the transport of Bi^{3+} ions during the catalyst electrodeposition process. In the ICRFBs, the electrolytes are transported from the channels into the porous electrodes by convection and diffusion. Due to the low diffusivity and low concentration of Bi^{3+} ions, the Bi^{3+} ion flux driven by

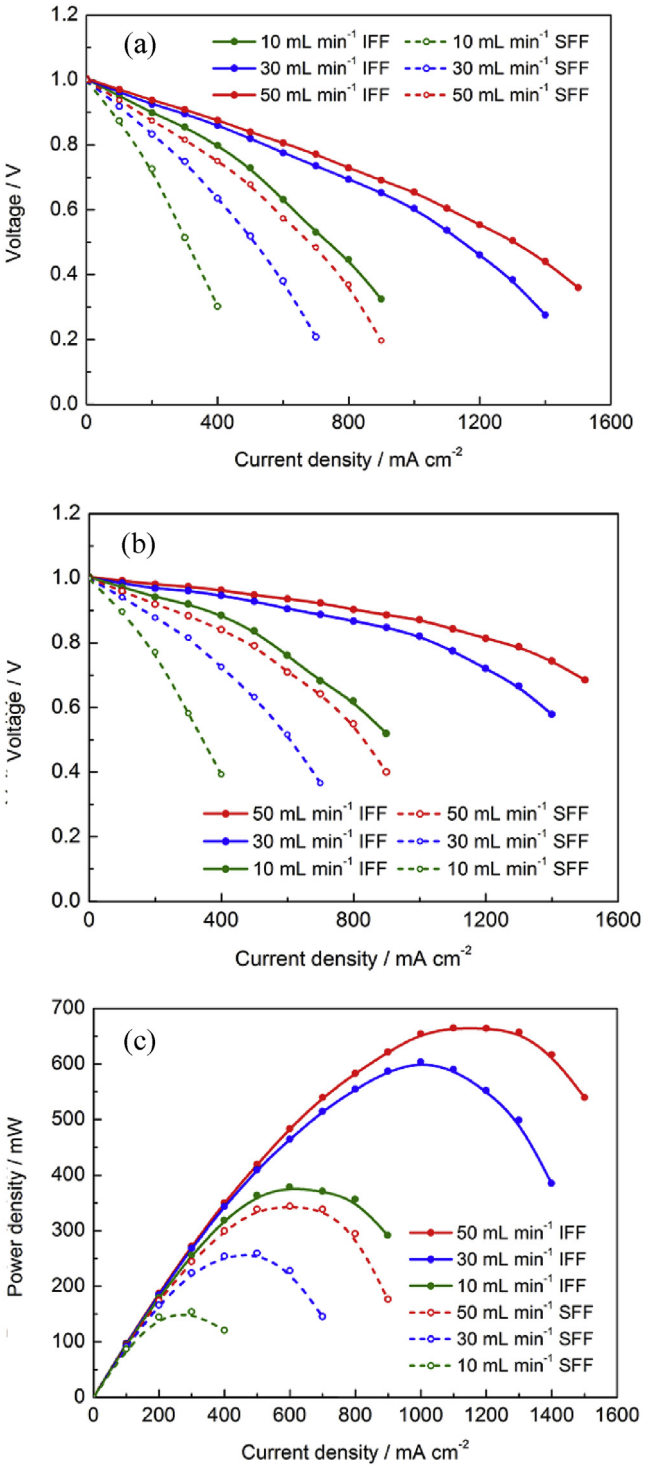

Fig. 5. (a) Discharge cell voltage, (b) IR-free discharge cell voltage and (c) output power density versus current density for the ICRFBs with IFFs and SFFs at various flow rates.

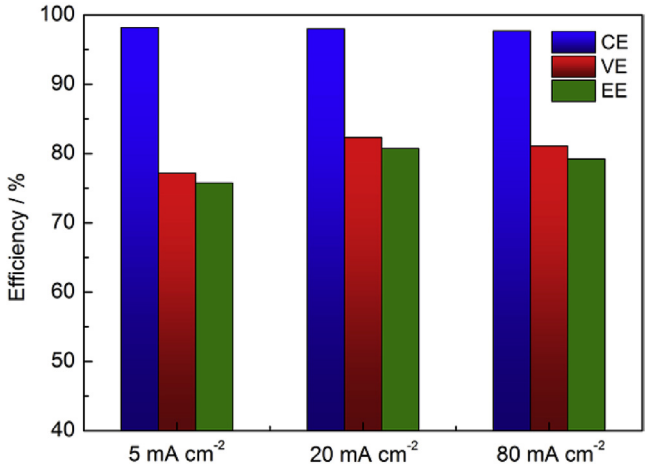

Fig. 6. The effect of the current density of catalyst electrodeposition on the battery performance.

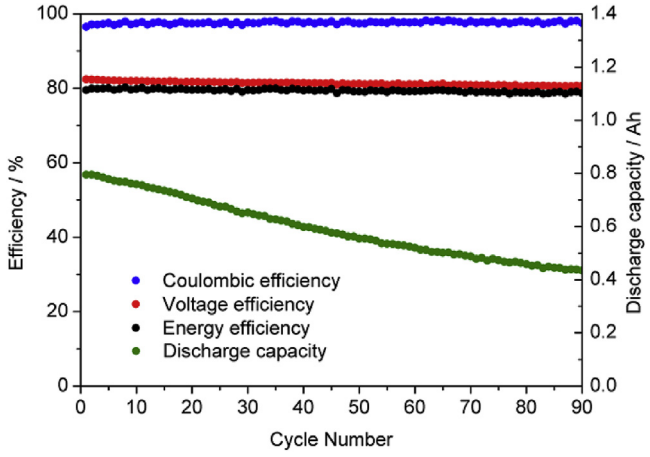

Fig. 7. Cycle performance of the ICRFB with IFFs at 320 mA cm^{-2}.

diffusion is quite limited. As shown in Fig. 1, the IFF design has non-continuous flow channels and forces all the electrolyte through the porous electrode between the neighboring inlet and outlet channels, thus providing strong forced convection. In the SFF design, the porous electrode hydraulically parallels to the flow field, and merely a portion of electrolyte flows through the porous electrode as the under-rib convection causing by the pressure drop between the two neighboring channels. Compared with the SFF design, the IFF design generally provides higher pressure drop between the two neighboring channels and stronger convective transport of species in the porous electrode [40].

As shown in Fig. 2a, the electrode near the current collector of the ICRFB with the IFF has a more uniform catalyst distribution from the under-channel to under-rib regions, characterized by SEM images and Bi element mappings. According to the EDX mappings of Fig. 2a, the bismuth amount of the IFF based ICRFB is significantly higher than that of the SFF based ICRFB at the under-rib region. The result indicates that the ICRFB with IFFs has better mass transport at the under-rib region of near-current-collector electrode compared to the ICRFB with SFFs. Fig. 2b shows the under-channel regions of the electrodes near the membrane. It is found that the ICRFB with the SFF has extremely low catalyst loading on the electrode near the membrane due to the limited mass transport. According to the element analysis by EDX mapping, the atomic ratio of Bi/C element is 1.006% for the near-membrane electrode of the ICRFB with the IFF, while it is merely 0.031% for that of the ICRFB with the SFF. Compared with the SFF design, the IFF design achieves higher catalyst loading at the electrode near the membrane, which is resulted by the stronger convection of the IFF design.

Fig. 3a shows the EIS of the ICRFBs with the IFF and SFF at the open-circuit condition (50% SOC). The internal resistance of the batteries are almost the same. The ICRFB with the IFF has significantly smaller semicircle compared with that with the SFF, which

indicates the ICRFB with the IFF has smaller activation loss. This result is consistent with the IR-free charge-discharge polarization curve shown in Fig. 3b. At the region of low current densities that the mass transport loss is negligible, the ICRFB with the IFF shows smaller polarizations, indicating that the ICRFB with the IFF has smaller activation loss.

3.2. Charge-discharge performance

The charge-discharge performance of the ICRFB with the IFF is shown in Fig. 4a–b. The coulombic efficiencies of the two ICRFBs are almost identical. The voltage efficiency of the ICRFB with the IFF is 95.2% at 80 mA cm^{-2}, which is 2.8% higher than that of the ICRFB with the SFF (92.4%). The voltage efficiency of the ICRFB with the IFF still remains 86.4% at 240 mA cm^{-2}. As shown in Fig. 4b, at 240 mA cm^{-2}, the discharge curve of the ICRFB with the IFF is approximately 67 mV higher than that of the ICRFB with the SFF, while the charge curve of the ICRFB with the IFF is 79 mV lower than that of the ICRFB with the SFF. At a higher current density of 320 mA cm^{-2}, the energy efficiency of the ICRFB with the IFF is 80.7%, significantly higher than that of the ICRFB with the SFF (72.5%). Based on Figs. 3b and 5a–b, the polarization curves and IR-free polarization curves of both the IFF and SFF based ICRFBs at current densities of 80–320 mA cm^{-2} are almost linear, which indicates that the mass transport loss is small within these current densities. Therefore, we infer that the dominant reason for the improved energy efficiency at 80–320 mA cm^{-2} is the more uniform catalyst distribution. At the identical energy efficiency of approximately 80%, the operating current density of the ICRFB with the IFF dramatically increases from 200 to 320 mA cm^{-2} compared to the ICRFB with the SFF. The higher current density means smaller cell stacks and lower cost for the same power requirement.

In addition to the more uniform distribution of Bi catalyst, the improved performance of the ICRFB with the IFF is also attributed to the enhanced mass transport of active species in the porous electrode, especially at high current densities (>600 mA cm^{-2}). According to the full-scale discharge polarization curves illustrated in Fig. 5a–b, the ICRFB with the IFF has remarkably higher performance compared to the ICRFB with the SFF, especially at high current densities. At the same flow rate, the influence of mass transport on the ICRFB with the IFF appears at higher current densities compared to the ICRFB with the SFF, indicating that the ICRFB with the IFF has smaller mass transport loss (higher mass transport limitation). As illustrated in Fig. 5c, the peak power density of the ICRFB with the IFF reaches 665 mW cm^{-2} at 50 mL min^{-1}, 93% higher than that of the ICRFB with the SFF (344 mW cm^{-2}). With such a high power density, intrinsically low-cost active materials and non-precious Bi catalyst, the ICRFB with the IFF is expected to have strong competitiveness in the large-scale energy storage field.

The current density of catalyst electrodeposition should have influence on the catalyst electrodeposition and battery performance. The ICRFBs with the IFF have been tested at electrodeposition current densities of 5, 20 and 80 mA cm^{-2}. Then the charge-discharge tests are conducted at 320 mA cm^{-2}, and used to evaluate the battery performance [41]. As shown in Fig. 6, the ICRFB with 20 mA cm^{-2} electrodeposition delivers the highest voltage efficiency as well as the highest energy efficiency. This is because that too high electrodeposition current density causes the uneven distribution of catalyst in the porous electrode. On the other hand, with the electrodeposition current density decreasing, the overpotential of the catalyst electrodeposition decreases, and the number of the activated nucleation sites for catalyst growth decreases, which leads to the larger catalyst particle size and smaller active catalytic surface [42].

3.3. Cycle performance

The stability of ICRFBs is of great significance for the practical application. It is desirable that the battery can work stably and have a small capacity decay rate. The cycle test is conducted at 320 mA cm^{-2} and 65 °C with the voltage window of 0.8–1.2 V. The 50 mL electrolytes with a theoretical capacity of 1.34 Ah are used as both positive and negative electrolytes. As presented in Fig. 7, the voltage efficiency, coulombic efficiency and energy efficiency of the ICRFB with the IFF are stable. The capacity decay rate is 0.5% per cycle, significantly lower than that of the reported ICRFB [18]. The decayed capacity can be recovered by the rebalancing process [25].

4. Conclusions

In summary, the effects of the flow field design on the catalyst electrodeposition and battery performance are investigated, and characterized by the SEM image and EDX mapping, EIS, polarization curve, charge-discharge curve. With the forced convection of electrolyte in the porous electrode, the IFF design enhances transport of Bi^{3+} in the porous electrode during the catalyst electrodeposition, enables a more uniform catalyst distribution, and reduces the activation loss compared with the SFF design. Moreover, the ICRFB with the IFF exhibits higher mass transport limitation. It is demonstrated that the ICRFB with the IFF achieves a high current density of 320 mA cm^{-2} with the energy efficiency above 80%, which renders the ICRFB outstanding competitiveness for large-scale energy storage.

Acknowledgements

The work described in this paper was fully supported by a grant from the Research Grants Council of the Hong Kong Special Administrative Region, China (Project No. 623313).

References

[1] B. Li, M. Gu, Z. Nie, Y. Shao, Q. Luo, X. Wei, X. Li, J. Xiao, C. Wang, V. Sprenkle, Bismuth nanoparticle decorating graphite felt as a high-performance electrode for an all-vanadium redox flow battery, Nano Lett. 13 (2013) 1330–1335.
[2] W. Wang, Q. Luo, B. Li, X. Wei, L. Li, Z. Yang, Recent progress in redox flow battery research and development, Adv. Funct. Mater. 23 (2013) 970–986.
[3] Z. Yang, J. Zhang, M.C. Kintner-Meyer, X. Lu, D. Choi, J.P. Lemmon, J. Liu, Electrochemical energy storage for green grid, Chem. Rev. 111 (2011) 3577–3613.
[4] B. Huskinson, M.P. Marshak, C. Suh, S. Er, M.R. Gerhardt, C.J. Galvin, X. Chen, A. Aspuru-Guzik, R.G. Gordon, M.J. Aziz, A metal-free organic-inorganic aqueous flow battery, Nature 505 (2014) 195–198.
[5] K.L. Hawthorne, J.S. Wainright, R.F. Savinell, Studies of iron-ligand complexes for an all-iron flow battery application, J. Electrochem. Soc. 161 (2014) A1662–A1671.
[6] M.C. Wu, M.Y. Liu, G.F. Long, K. Wan, Z.X. Liang, T.S. Zhao, A novel high-energy-density positive electrolyte with multiple redox couples for redox flow batteries, Appl. Energy 136 (2014) 576–581.
[7] K. Gong, X. Ma, K.M. Conforti, K.J. Kuttler, J.B. Grunewald, K.L. Yeager, M.Z. Bazant, S. Gu, Y. Yan, A zinc–iron redox-flow battery under $100 per kw h of system capital cost, Energy Environ. Sci. 8 (2015) 2941–2945.
[8] M.C. Tucker, K.T. Cho, A.Z. Weber, Optimization of the iron-ion/hydrogen redox flow cell with iron chloride catholyte salt, J. Power Sources 245 (2014) 691–697.
[9] K. Lin, Q. Chen, M.R. Gerhardt, L. Tong, S.B. Kim, L. Eisenach, A.W. Valle, D. Hardee, R.G. Gordon, M.J. Aziz, Alkaline quinone flow battery, Science 349 (2015) 1529–1532.
[10] X.L. Zhou, T.S. Zhao, L. An, Y.K. Zeng, X.H. Yan, A vanadium redox flow battery model incorporating the effect of ion concentrations on ion mobility, Appl. Energy 158 (2015) 157–166.
[11] X.L. Zhou, T.S. Zhao, L. An, L. Wei, C. Zhang, The use of polybenzimidazole membranes in vanadium redox flow batteries leading to increased coulombic efficiency and cycling performance, Electrochim. Acta 153 (2015) 492–498.
[12] X.L. Zhou, Y.K. Zeng, X.B. Zhu, L. Wei, T.S. Zhao, A high-performance dual-scale porous electrode for vanadium redox flow batteries, J. Power Sources 325 (2016) 329–336.

[13] L. Wei, T.S. Zhao, G. Zhao, L. An, L. Zeng, A high-performance carbon nanoparticle-decorated graphite felt electrode for vanadium redox flow batteries, Appl. Energy 176 (2016) 74–79.
[14] L. Wei, T.S. Zhao, L. Zeng, X.L. Zhou, Y.K. Zeng, Titanium carbide nanoparticle-decorated electrode enables significant enhancement in performance of all-vanadium redox flow batteries, Energy Technol. (2016), http://dx.doi.org/10.1002/ente.201600016.
[15] Q. Liu, G. Grim, A. Papandrew, A. Turhan, T.A. Zawodzinski, M.M. Mench, High performance vanadium redox flow batteries with optimized electrode configuration and membrane selection, J. Electrochem. Soc. 159 (2012) A1246–A1252.
[16] P. Leung, J. Palma, E. Garcia-Quismondo, L. Sanz, M. Mohamed, M. Anderson, Evaluation of electrode materials for all-copper hybrid flow batteries, J. Power Sources 310 (2016) 1–11.
[17] L.H. Thaller, Electrically Rechargeable Redox Flow Cells, NASA TM X-71540, Lewis Research Centre, 1974.
[18] Y.K. Zeng, T.S. Zhao, L. An, X.L. Zhou, L. Wei, A comparative study of all-vanadium and iron-chromium redox flow batteries for large-scale energy storage, J. Power Sources 300 (2015) 438–443.
[19] L.H. Thaller, Recent Advances in Redox Flow Cell Storage Systems, NASA TM-79186, Lewis Research Centre, 1979.
[20] Q. Ye, J. Hu, P. Cheng, Z. Ma, Design trade-offs among shunt current, pumping loss and compactness in the piping system of a multi-stack vanadium flow battery, J. Power Sources 296 (2015) 352–364.
[21] N. Hagedorn, M. Hoberecht, L. Thaller, Nasa-redox Cell-stack Shunt Current, Pumping Power, and Cell-performance Tradeoffs, National Aeronautics and Space Administration, Cleveland, OH (USA), 1982. Lewis Research Center.
[22] R.M. Darling, M.L. Perry, The influence of electrode and channel configurations on flow battery performance, J. Electrochem. Soc. 161 (2014) A1381–A1387.
[23] M. Lopez-Atalaya, G. Codina, J. Perez, J. Vazquez, A. Aldaz, Optimization studies on a Fe/Cr redox flow battery, J. Power Sources 39 (1992) 147–154.
[24] R.F. Gahn, J. Charleston, J.S. Ling, M.A. Reid, Performance of Advanced Chromium Electrodes for the NASA Redox Energy Storage System, National Aeronautics and Space Administration, Cleveland, OH (USA), 1981. Lewis Research Center.
[25] R.F. Gahn, N.H. Hagedorn, J.A. Johnson, Cycling Performance of the Iron-Chromium Redox Energy Storage System, NASA TM-87034, Lewis Research Centre, 1985.
[26] Y.K. Zeng, X.L. Zhou, L. An, L. Wei, T.S. Zhao, A high-performance flow-field structured iron-chromium redox flow battery, J. Power Sources 324 (2016) 738–744.
[27] E. Hollax, D.S. Cheng, The influence of oxidative pretreatment of graphite electrodes on the catalysis of the Cr3+/Cr2+ and Fe3+/Fe2+ redox reactions, Carbon 23 (1985) 655–664.
[28] C. Wu, D. Scherson, E. Calvo, E. Yeager, M. Reid, A bismuth-based electrocatalyst for the chromous-chromic couple in acid electrolytes, J. Electrochem. Soc. 133 (1986) 2109–2112.
[29] C. Ding, H. Zhang, X. Li, T. Liu, F. Xing, Vanadium flow battery for energy storage: prospects and challenges, J. Phys. Chem. Lett. 4 (2013) 1281–1294.
[30] R.F. Gahn, N.H. Hagedorn, J.S. Ling, Single Cell Performance Studies on the Fe/Cr Redox Energy Storage System Using Mixed Reactant Solutions at Elevated Temperature, NASA TM-83385, Lewis Research Centre, 1983.
[31] C. Dennison, E. Agar, B. Akuzum, E. Kumbur, Enhancing mass transport in redox flow batteries by tailoring flow field and electrode design, J. Electrochem. Soc. 163 (2016) A5163–A5169.
[32] J. Houser, J. Clement, A. Pezeshki, M.M. Mench, Influence of architecture and material properties on vanadium redox flow battery performance, J. Power Sources 302 (2016) 369–377.
[33] S. Tsushima, S. Sasaki, S. Hirai, in: Proceedings of ECS Meeting, San Francisco, 2013, 1664–1664.
[34] Q. Xu, T.S. Zhao, P.K. Leung, Numerical investigations of flow field designs for vanadium redox flow batteries, Appl. Energy 105 (2013) 47–56.
[35] D. Aaron, Q. Liu, Z. Tang, G. Grim, A. Papandrew, A. Turhan, T. Zawodzinski, M. Mench, Dramatic performance gains in vanadium redox flow batteries through modified cell architecture, J. Power Sources 206 (2012) 450–453.
[36] Q. Xu, T.S. Zhao, C. Zhang, Performance of a vanadium redox flow battery with and without flow fields, Electrochim. Acta 142 (2014) 61–67.
[37] L. An, T.S. Zhao, X.L. Zhou, X.H. Yan, C.Y. Jung, A low-cost, high-performance zinc–hydrogen peroxide fuel cell, J. Power Sources 275 (2015) 831–834.
[38] A.M. Pezeshki, J.T. Clement, G.M. Veith, T.A. Zawodzinski, M.M. Mench, High performance electrodes in vanadium redox flow batteries through oxygen-enriched thermal activation, J. Power Sources 294 (2015) 333–338.
[39] Y.K. Zeng, P. Fan, X. Zhang, C. Fu, J. Li, G. Li, Sensitivity analysis for a planar sofc: size effects of the porous gas diffusion layer underneath the channel rib, Fuel Cells 14 (2014) 123–134.
[40] T.J. Latha, S. Jayanti, Hydrodynamic analysis of flow fields for redox flow battery applications, J. Appl. Electrochem. 44 (2014) 995–1006.
[41] Q. Zheng, F. Xing, X. Li, T. Liu, Q. Lai, G. Ning, H. Zhang, Investigation on the performance evaluation method of flow batteries, J. Power Sources 266 (2014) 145–149.
[42] V. Richoux, S. Diliberto, C. Boulanger, J. Lecuire, Pulsed electrodeposition of bismuth telluride films: influence of pulse parameters over nucleation and morphology, Electrochim. Acta 52 (2007) 3053–3060.